Matter

CellPress

Article

Identifying infectiousness of SARS-CoV-2 by ultra-sensitive SnS_2 SERS biosensors with capillary effect

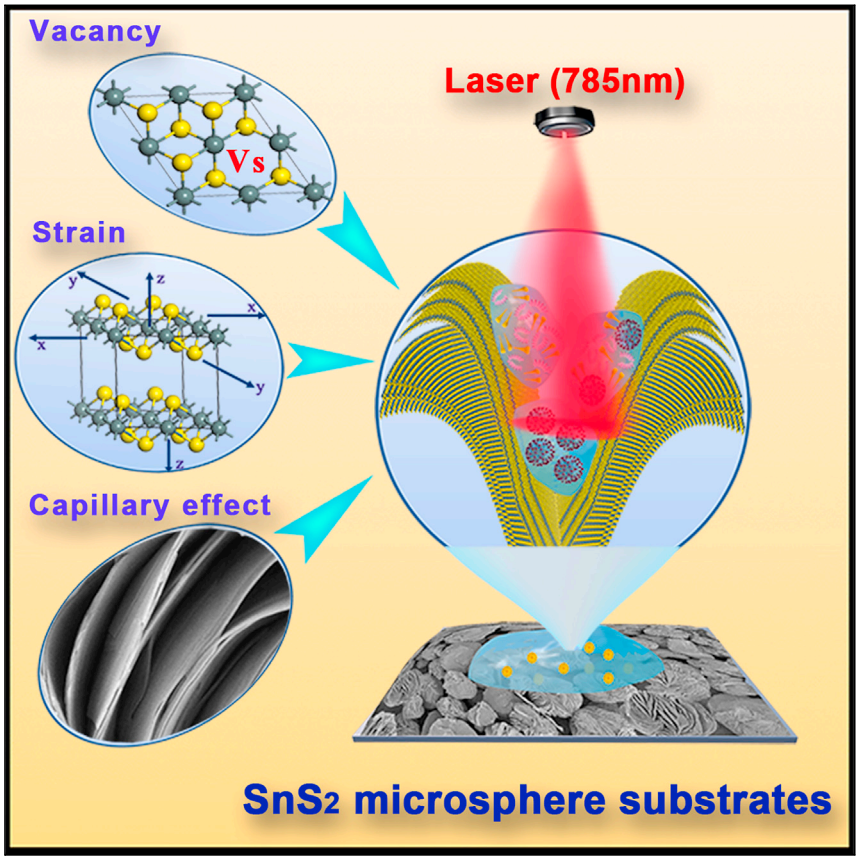

Motivated by the synergistic contribution of the molecular enrichment caused by capillary effect and the chemical enhancement boosted by lattice strain and sulfur vacancies, the developed ultra-sensitive SnS_2 hierarchical nanostructure SERS substrates exhibit an extremely low limit of detection of 10^{-13} M, which can be applied to complete the identification of infectiousness for SARS-CoV-2 samples, whereas the current PCR methods cannot.

Yusi Peng, Chenglong Lin, Yanyan Li, ..., Jianjun Liu, Xiaoying Luo, Yong Yang

yangyong@mail.sic.ac.cn

Highlights

Development of SnS_2 microsphere SERS substrates with ultra-low LOD of 10^{-13} M

Molecular enrichment is caused by capillary effect

Chemical enhancement is boosted by the lattice strain and sulfur vacancies

Completing the identification of infectiousness for SARS-CoV-2 samples

Peng et al., Matter 5, 694–709
February 2, 2022
https://doi.org/10.1016/j.matt.2021.11.028

6 **Development**
Practical, real world, technological considerations and constraints

CellPress

Matter

Article

Identifying infectiousness of SARS-CoV-2 by ultra-sensitive SnS_2 SERS biosensors with capillary effect

Yusi Peng,[1,2,3] Chenglong Lin,[1,2,3] Yanyan Li,[1,2,3] Yong Gao,[4] Jing Wang,[4] Jun He,[5,6] Zhengren Huang,[1] Jianjun Liu,[1] Xiaoying Luo,[7] and Yong Yang[1,3,8,*]

SUMMARY

The current COVID-19 pandemic urges us to develop ultra-sensitive surface-enhanced Raman scattering (SERS) substrates to identify the infectiousness of SARS-CoV-2 virions in actual environments. Here, a micrometer-sized spherical SnS_2 structure with the hierarchical nanostructure of "nano-canyon" morphology was developed as semiconductor-based SERS substrate, and it exhibited an extremely low limit of detection of 10^{-13} M for methylene blue, which is one of the highest sensitivities among the reported pure semiconductor-based SERS substrates. Such ultra-high SERS sensitivity originated from the synergistic enhancements of the molecular enrichment caused by *capillary effect* and the charge transfer chemical enhancement boosted by the lattice strain and sulfur vacancies. The novel two-step SERS diagnostic route based on the ultra-sensitive SnS_2 substrate was presented to diagnose the infectiousness of SARS-CoV-2 through the identification standard of SERS signals for SARS-CoV-2 S protein and RNA, which could accurately identify non-infectious lysed SARS-CoV-2 virions in actual environments, whereas the current PCR methods cannot.

INTRODUCTION

Coronavirus disease 2019 (COVID-19), caused by SARS-CoV-2, is a serious threat to human health, where we are facing the dilemma of globalization and time continuity.[1,2] Since July 2020, identification of SARS-CoV-2 virions on cold chain items has been frequently reported in China and other countries, causing great concern on relevant virus transmission. It can be attributed to the fact that SARS-COV-2 can survive more than 3 weeks below 0°C during cold chain transportation.[3,4] It is important to note that a portion of SARS-COV-2 virions in the colder environment are lysed, inactive viruses. But the RNA of lysed SARS-CoV-2 might remain and easily be detected by the universally applied polymerase chain reaction (PCR) method,[5] resulting in the misdiagnosis of infectiousness for SARS-CoV-2, causing unnecessary social panic. Therefore, it is much more meaningful to determine whether the virus is infectious as identified on contaminated items in various environments.[6] However, exploiting a rapid and highly sensitive detection method that can identify lysed, non-infectious SARS-CoV-2 virions to rule out the contamination of infectious SARS-CoV-2 virus is a key scientific challenge.

Surface-enhanced Raman scattering (SERS), a single-molecule spectral detection technology, is currently expanding its promising applications from environmental science[7] and food safety[8,9] toward the biosensing field[10] due to its advantages of

Progress and potential

As the COVID-19 epidemic has swept the world, exploiting a rapid and highly sensitive detection method that can identify the infectiousness of SARS-CoV-2 virus and exclude the interference on diagnostic results and false alarms of the non-infectious SARS-CoV-2 virions has become a key scientific challenge. In this work, we designed a micrometer-sized spherical SnS_2 structure with the hierarchical nanostructure of "nano-canyon" morphology as an ultra-sensitive SERS substrate to groundbreakingly rapidly detect and identify the infectiousness of SARS-CoV-2 samples on site, which exhibits vital timeliness in patient management that the viral culture method does not have. It is significant to avoid misdiagnosing infectious SARS-CoV-2 in some contaminated patient gathering places.

ultra-high sensitivity, non-destructiveness, excellent repeatability, and accuracy. Motivated by the development of SERS technology, the direct non-labeled detection of various biological samples, such as adenovirus, animal viruses, HIV, and influenza virus, has been successfully developed.[10–14] With respect to SARS-CoV-2 virus, Yeh group[15] reported that an Au nanoparticle microfluidic platform was successfully established for rapid and label-free capturing and SERS detection of viruses. In our previous work,[16] an ACE2-modified SERS sensor was reported to exhibit a low limit of detection (LOD) of 80 copies/mL for the SARS-CoV-2 in contaminated wastewater in as short as 5 min. In addition, Choo and Ray group[17,18] applied deoxyribonucleic acid aptamers and viral anti-spike antibodies as receptors to achieve sensitive SERS detection of SARS-CoV-2, and their detection limits reached 10 PFU/mL and 18 copies/mL, respectively. These reports indicated that SERS technology could be developed into a potential method for virus detection. In the SERS biosensor field, to pursue more excellent biocompatibility with biological samples and excellent spectral stability and reproducibility, SERS substrates are now actively being expanded from noble metals to semiconductor materials.[19] Recently, Lin[20] reported that MCF-7 drug-resistant breast cancer cells could be accurately identified based on highly sensitivity B-TiO_2 SERS substrates, which widened the application of semiconductor-based SERS platforms in precise diagnosis of cancer. However, compared with SERS spectra of biological samples mainly originated from electromagnetic enhancement, the SERS enhancement of semiconductor-based substrates is relatively weak[21] because it is difficult for the semiconductor-based substrates, in which charge transfer plays a major role, to significantly enhance the chemical bond vibration of the entire biological molecule due to their larger molecular size. Therefore, a top-priority task is to achieve ultra-high SERS sensitivity in semiconductor-based substrates, which can even parallel noble metals with *hot spots*.

With respect to semiconductor-based substrates, the probability of electronic transition ω_{lk} can be expressed by Fermi's golden rule: $\omega_{lk} = \frac{2\pi}{\hbar} g(E_k)\left|H'_{kl}\right|^2$, where $g(E_k)$ is the electronic density of states, and H'_{kl} represents the matrix of electronic transitions on the highest occupied molecular orbital (HOMO)-lowest unoccupied molecular orbital (LUMO).[22] Therefore, the SERS sensitivity of semiconductor-based substrates contributed by the charge transfer between probe molecules and semiconductors can be optimized by the following two aspects: (1) increasing the electronic density of states $g(E_k)$ near the Fermi level of semiconductor materials to enhance the chemical bond vibrations of molecules and (2) regulating the HOMO and LUMO orbitals of semiconductors to realize the larger probability of charge transfer to significantly enhance the molecular chemical bond vibrations.[23–25] In general, the electronic structures of semiconductors can be modulated by element doping,[23,26] introducing vacancies,[27,28] applying external strain fields,[29] and constructing heterojunctions[30] and amorphous substrates.[31] Although motivated by above optimized strategies for SERS performance, the LODs of pure semiconductor-based substrates in most previous publications are still universally lower than 10^{-10} M level, which is a new bottleneck encountered by semiconductor substrates. SnS_2, as a typical two-dimensional layered structure, has a bandgap that varies from 1 to 3 eV with the thickness and morphology of nanosheets. Sulfur vacancies that easily exist on the surface of SnS_2 nanosheets are conductive to induce the intermediate energy level near the Fermi level to promote electronic transitions,[32,33] making them a promising candidate for SERS substrates. However, there are few reports on the SERS applications of SnS_2.[34] Here, an ultra-high SERS sensitivity of SnS_2 nanosheets is realized by simultaneously introducing sulfur vacancies and generating lattice strain through regulating morphology, thereby satisfying sensitivity requirements of a SERS biosensor for the detection of SARS-CoV-2 and other biomolecules.

[1]State Key Laboratory of High-Performance Ceramics and Superfine Microstructures, Shanghai Institute of Ceramics, Chinese Academy of Sciences, 1295 Dingxi Road, Shanghai 200050, People's Republic of China

[2]University of Chinese Academy of Sciences, No.19(A) Yuquan Road, Beijing 100049, People's Republic of China

[3]Center of Materials Science and Optoelectronics Engineering, University of Chinese Academy of Sciences, Beijing 100049, China

[4]The First Affiliated Hospital of USTC, Division of Life Sciences and Medicine, University of Science and Technology of China, Hefei, Anhui 230001, China

[5]Anhui Provincial Center for Disease Control and Prevention, Hefei, Anhui 12560, China

[6]Public Health Research Institute of Anhui Province, Hefei, Anhui 12560, China

[7]State Key Laboratory of Oncogenes and Related Genes, Shanghai Cancer Institute, Renji Hospital, Shanghai Jiaotong University School of Medicine, Shanghai 200032, China

[8]Lead contact

*Correspondence: yangyong@mail.sic.ac.cn

https://doi.org/10.1016/j.matt.2021.11.028

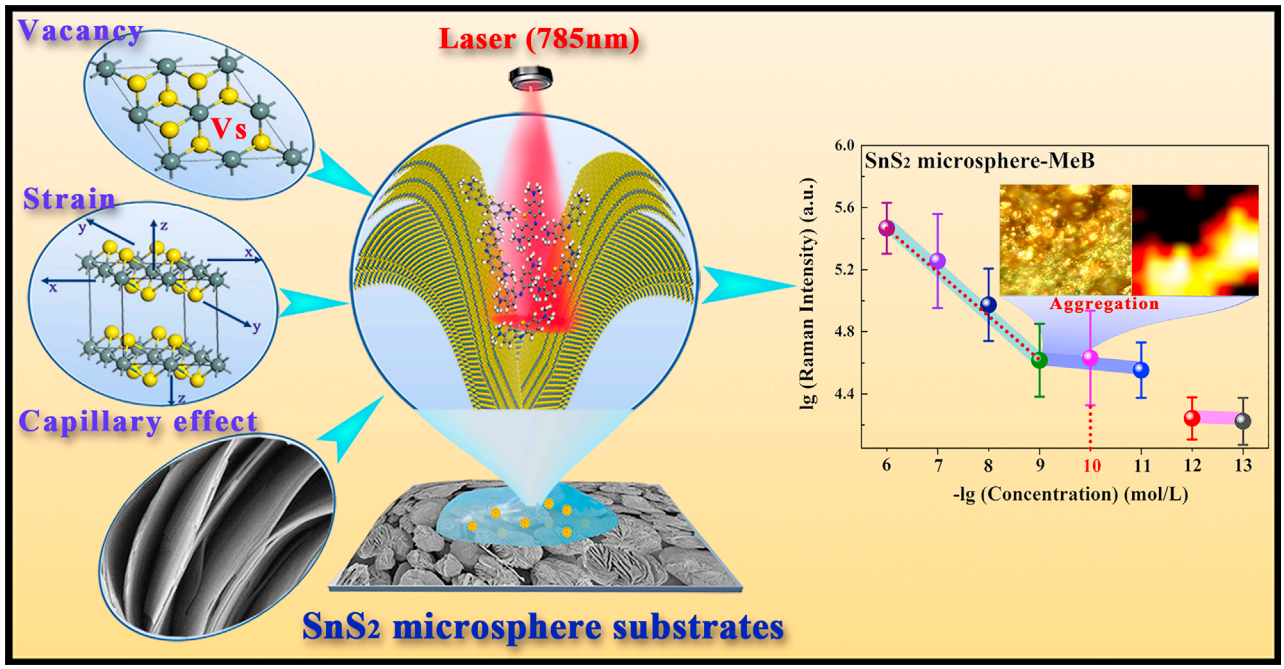

Figure 1. Schematic diagram of SnS_2 microsphere substrates design and the ultra-sensitive SERS performance

In this work, we designed a micrometer-sized spherical SnS_2 structure with the hierarchical nanostructure of "nano-canyon" morphology. Benefiting from this unique nano-canyon structure, the molecular enrichment caused by *capillary effect* was generated on the surface of SnS_2 microspheres, where the existence of the lattice strain and sulfur vacancies can further boost the chemical enhancement by stimulating a larger probability of charge transfer. Motivated by the synergistic contribution of the above three components to the SERS enhancement (Figure 1), the enhancement factor for methylene blue (MeB) can reach up to 3.0×10^8, and its LOD as low as 10^{-13} M, which is not only much better than most reported pure semiconductor-based SERS substrates, but it also breaks the newly encountered bottleneck of LOD of 10^{-10} M. Based on this ultra-sensitive SERS detection ability of SnS_2 microspheres, the ultra-high SERS sensitivity endowed SnS_2 microspheres with the capability to groundbreakingly detect and identify the infectiousness of SARS-CoV-2 based on the identification standard of SERS signals for SARS-CoV-2 S protein and RNA, which could accurately identify non-infectious lysed SARS-CoV-2 virions, whereas the current PCR methods cannot. It is significant to avoid misdiagnosing infectious SARS-CoV-2 in actual environments.

RESULTS AND DISCUSSION

Characterization of SnS_2 microsphere

The shape-controlled SnS_2 microspheres were first synthesized through a simple one-step hydrothermal reaction, and the schematic illustration of the synthetic process is shown in Figure 2A. Briefly, the determined concentrations of thioacetamide (TTA) and sodium stannate (Na_2SnO_3) served as the sulfur source and the tin source, respectively. The X-ray powder diffraction (XRD) pattern in Figure S1A shows that the synthesized brown powder was crystallized with SnS_2 phase (PDF#75-0367) with lattice constants corresponding to the hexagonal structure with space group $P\bar{3}m1$ (a = 3.65 Å, b = 3.65 Å, c = 5.90 Å). In a hexagonal SnS_2 unit cell, a single Sn atom was covalently bonded to six atoms of S in the octahedral sites of individual layers[35]

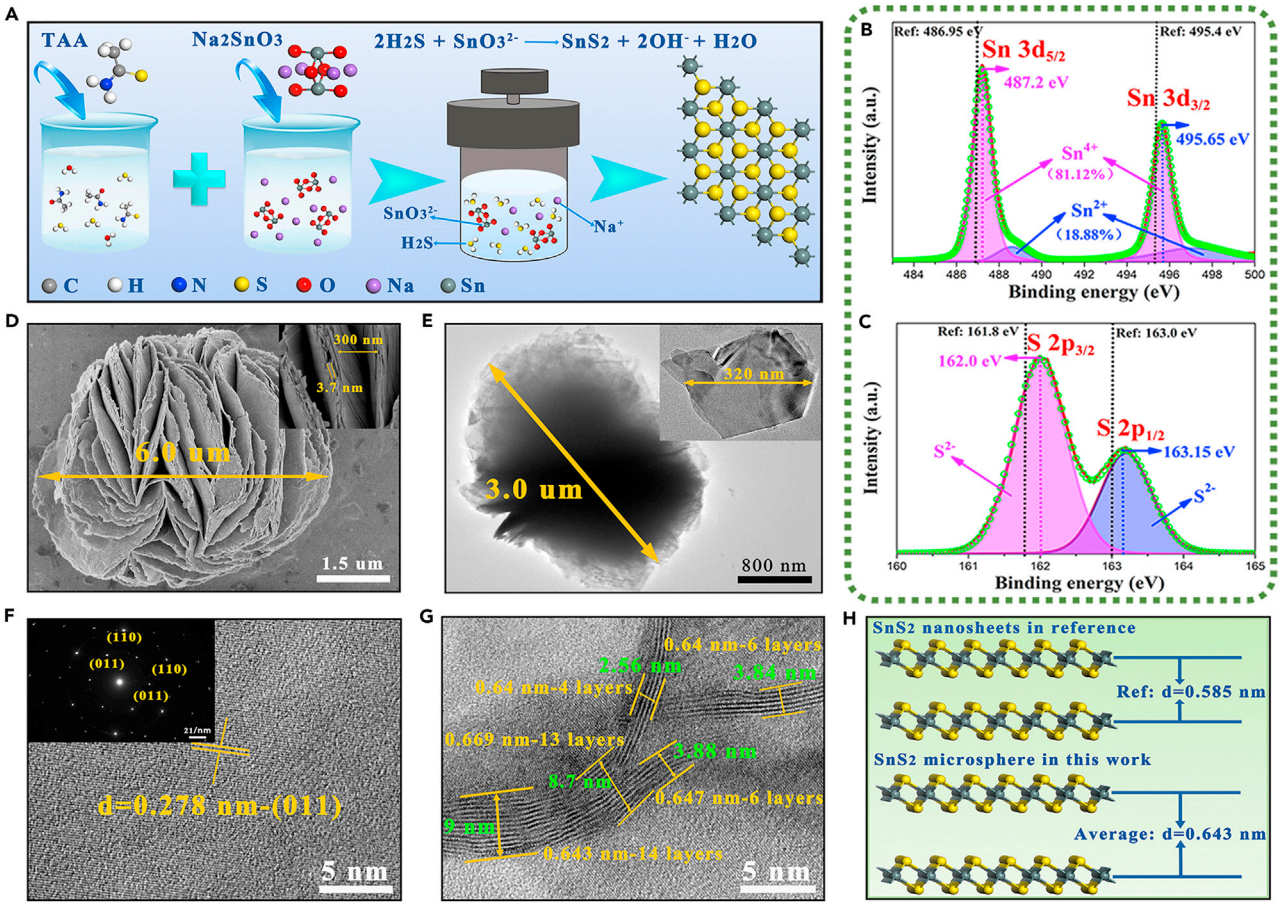

Figure 2. Synthesis, crystal phase, morphology, and structure characterization of SnS_2 microspheres

(A) Schematics illustrating the synthesis of SnS_2 microspheres.

(B and C) Sn*3d* and S*2p* XPS spectrum.

(D) SEM images.

(E) TEM images.

(F) HRTEM images.

(G) HRTEM images of cross-section for nanosheets.

(H) Crystal structure diagram.

(Figure 2A). The strongest peak indexed to (011) indicated the exposed crystal plane of SnS_2 is (011). Additionally, the diffraction peaks corresponding to the (001), (100), and (011) crystal planes all shift to lower angles (Figure S1B and S1C), which indicated the entire crystal lattice of hexagonal SnS_2 structure was increased, especially with an increase in interlayer distance. It could be attributed to the fact that the typical layered structure of SnS_2 was composed of a three-layered stacked atomic layer (S–Sn–S) connected by van der Waals forces, which was susceptible to generate lattice strain caused by regulating SnS_2 morphology. Raman spectra is a perfect method to explore the changes in interlayer distance of SnS_2 structure. As shown in Figure S2, the distinct Raman peak at 315 cm^{-1} was assigned to the vertical plane vibration mode (A_{1g}) of Sn–S bonds. This Raman peak of A_{1g} mode exhibited an obvious red shift in relation to the Raman shift of 312 cm^{-1} reported in the literature,[34,36] which also demonstrated the increase in interlayer distance of SnS_2 structure. It was mainly attributed to the decrease in van der Waals interactions between the interlayers, resulting in the decrease in restoring forces on atoms.[37,38] XPS spectra in Figures 2B and 2C shows that Sn and S could be clearly identified in

SnS_2 samples, among which both Sn*3d* and S*2p* peaks presented a significant shift to the higher binding energy in relation to reported literature,[33,35] indicating the changed electron density difference of SnS_2 affected by the lattice strain. In addition to the doublet peaks at 487.2 eV (Sn$3d_{5/2}$) and 495.7 eV (Sn$3d_{3/2}$) arising from Sn^{4+}, there was also a pair of weaker doublet peaks at 488.7 eV (Sn$3d_{5/2}$) and 497.5 eV (Sn$3d_{3/2}$), which belonged to Sn^{2+} (Sn^{4+}:Sn^{2+} ≈ 4:1), indicating the presence of sulfur vacancy (V_S). Additionally, the enlarged characteristic peaks in the S*2p* region of SnS_2 at 162.0 and 163.2 eV were both attributed to S^{2+}. Moreover, there were no S*2p* peaks between 168 and 170 eV (Figure S3), suggesting that SnS_2 was barely oxidized to SnO_2.

Then scanning electron microscopy (SEM) and transmission electron microscopy (TEM) were used to study the morphology of SnS_2. The low-magnification SEM image (Figure S4) shows that the SnS_2 products exhibited a special spherical morphology with the statistical average size of 5.37 μm, which could be called a SnS_2 microsphere. The further analysis of high-magnification morphology (Figure 2D) revealed the existence of hierarchical nanostructures on the microsphere surface, and SnS_2 microspheres were formed by this hierarchical nanostructure of curling, stacked nanosheets. Furthermore, this hierarchical nanostructure resulted in a special morphology that was similar to a bottomless *canyon* with wide top and narrow bottom, where the width of these nano-canyons was mostly less than 300 nm. Compared with the reported SnS_2 nanostructures such as nanoflowers, nanobelts, and nanosheets,[32,35,36] this unique morphology of SnS_2 with the hierarchical nanostructure was reported for the first time to our knowledge, and it was expected to exhibit surprisingly ultra-high sensitivity in the SERS detection field. The TEM image in Figure 2E also demonstrates the spherical morphology with micron-level size, and the shedding nanosheets that formed the hierarchical nanostructure possess a transverse size of about 300 nm. Moreover, there are no other impurity signals in the energy-dispersive X-ray spectroscopy other than the S and Sn signals, which demonstrated the high purity of the synthesized SnS_2 microspheres (as shown in Figure S5). Selected area electron diffraction (SAED) and high-resolution TEM (HRTEM) were used to analyze the crystal structure of the SnS_2 microspheres (Figure 2F). The clear lattice fringes on SnS_2 nanosheets were easily discerned by HRTEM to correspond to the (011) planes of hexagonal structures with an inter-planar spacing of 0.278 nm, which is consistent with the exposed crystal plane obtained from XRD results. The SAED pattern also confirmed the high crystallinity and the hexagonal symmetry structure of SnS_2 nanosheets. The cross-section morphology of SnS_2 microspheres was adopted to further analyze the detailed information of the thickness and interlayer distance of SnS_2 nanosheets. According to the HRTEM and crystal structure diagram of hexagonal SnS_2 (Figures 2G, 2H, and S6), the thickness of the single-layer SnS_2 nanosheet-formed hierarchical nanostructure was mostly less than 4 nm, which is equivalent to the thickness of 6 atomic layers for hexagonal SnS_2. Therefore, the average interlayer distance of SnS_2 microspheres was about 0.643 nm, which was far larger than the interlayer distance of 0.59 nm reported in the literature.[32,35,36] Moreover, the larger interlayer distance of 0.669 nm existed at the bend in SnS_2 nanosheets, indicating a larger lattice strain. This conclusion confirmed the existence of lattice strain in the SnS_2 microspheres once again.

Raman enhancement for SnS_2 microspheres

Following extensive research on SnS_2 nanostructures with various morphologies, the synthesized SnS_2 microspheres with a unique hierarchical nanostructure showed immense attraction for researchers in the photocatalysis and batteries fields, especially in the SERS detection field. The conventional MeB probe molecule was

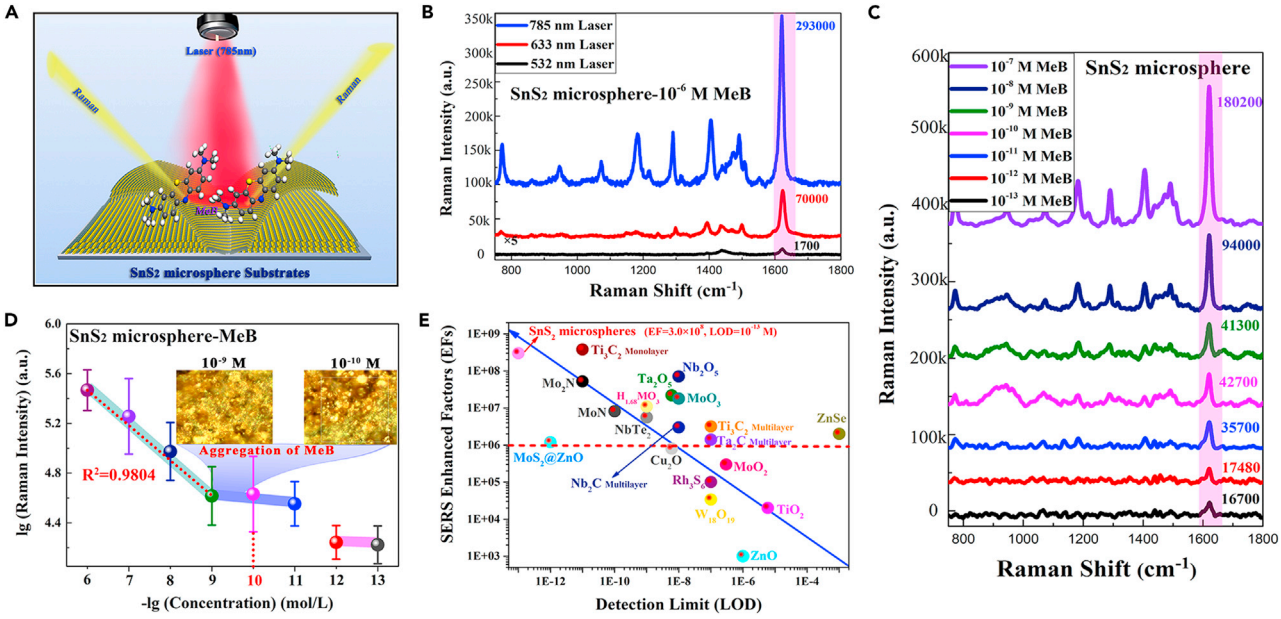

Figure 3. SERS performance of SnS_2 microspheres

(A) Raman scattering diagram of MeB and SnS_2 substrate.

(B) Raman spectra of 10^{-6} M MeB on SnS_2 microspheres under the excitation laser of 532 nm, 633 nm, and 785 nm.

(C) Raman spectra of MeB with concentration of 10^{-7}–10^{-13} M on SnS_2 microspheres.

(D) Raman intensity of MeB on SnS_2 microspheres at 1,620 cm^{-1} as a function of its concentration of 10^{-6}–10^{-13} M.

(E) Comparison of SERS performance of different reported semiconductor-based substrates.

adopted to examine the SERS performance of SnS_2 microspheres because MeB exhibited a strong optical absorption peak in the visible light region (Figure S7). The Raman scattering diagram of MeB and SnS_2 substrate is presented in Figure 3A. First, we investigated the optimal excitation wavelength of SnS_2 microspheres on MeB molecules. Raman spectra in Figure 3B show that MeB molecules on SnS_2 microspheres had an obviously stronger Raman enhancement with the excitation laser of 785 nm than that of the other two excitation lasers of 532 nm and 633 nm. Interestingly, the optimal excitation wavelength of 785 nm is the most popular wavelength of biological Raman detection, which lays a foundation for the bio-detection application of SnS_2 microspheres. Under the irradiation of a 785-nm laser, all Raman peaks of MeB molecules were significantly enhanced, especially in the Raman vibration mode of the asymmetric stretching vibration of benzene rings at the main peak of 1,620 cm^{-1}. All these enhanced Raman peaks of MeB and their corresponding Raman vibration modes are listed in Table S1.

Surprisingly, even if the MeB molecules were diluted to an extremely low molar concentration of 10^{-13} M, an obvious Raman signal of MeB molecules could still be detected by adsorbing molecules to SnS_2 substrates (Figure 3C). The relationship trend of Raman intensity at 1,620 cm^{-1} changing with the MeB concentration of 10^{-6} to 10^{-13} M is shown in Figure 3D, and inset graphs show the optical magnification pictures of 10^{-9} and 10^{-10} M MeB molecules on SnS_2 microspheres. It was found that the linear relationship was satisfactory in the range of 10^{-6} to 10^{-9} M with the correlation coefficient of 0.9804. However, when the concentration of MeB was lower than 10^{-10} M, Raman intensity no longer decreased linearly with the decreased concentration of MeB molecules. The Raman intensity of MeB with lower than 10^{-10} M decreased little, which could be attributed to a strange phenomenon (inset graphs of Figure 3D) where the low-concentration MeB molecule adsorbed on SnS_2

microspheres substrates would automatically enrich during the drying and evaporation process. Beneficial to this enriching phenomenon of low-concentration molecules, the LOD of SnS_2 microspheres for MeB could be as low as 10^{-13} M, and the corresponding SERS enhancement factor at 1,620 cm^{-1} with the irradiation laser of 785 nm was determined to be 3.0×10^8 (calculation details are shown in SI-3 of the supplemental information). To the best of our knowledge, this SERS performance of SnS_2 microspheres is one of the highest sensitivities among the reported pure semiconductor-based SERS substrates (Figure 3E; Table S2), which can even parallel that of the noble metals with *hot spots*. Encouragingly, the extremely low SERS LOD of 10^{-13} M for SnS_2 microspheres not only breaks the newly encountered bottleneck of detection limits, but it also provides a competitive candidate for a SERS detection application of biomolecules. Additionally, the SERS-enhanced stability of SnS_2 microspheres was proved by detecting the Raman spectra of 10^{-7} M MeB on SnS_2 microspheres placed for 5 months (Figure S8). Compared with the Raman intensity of 10^{-7} M MeB on fresh SnS_2 substrates, the average Raman intensity of 10^{-7} M MeB on SnS_2 substrates after 5 months was only discounted 16.7%, and it still maintained a significant Raman enhanced effect. Such excellent SERS-enhanced stability has stimulated SnS_2 microspheres to exhibit a promising application prospect in the practical SERS detection of biomolecules. However, with respect to the explanations of enrichment phenomenon for low-concentration probe molecules on SnS_2 microspheres, it is worthwhile to further explore that in the following analysis of the SERS-enhanced mechanism.

SERS-enhanced mechanism of SnS_2 microspheres

As we expected from the above analysis, SnS_2 microspheres with hierarchical nanostructures exhibited ultra-sensitive SERS detection ability. Actually, the extremely low LOD mainly depends on the realization of enrichment phenomenon for low-concentration molecules on SnS_2 microspheres. The enrichment phenomenon of molecules is mainly controlled by the superficial microscopic morphology of materials. As seen in SEM images (Figure 2D), the hierarchical nanostructure with a unique *nano-canyon* morphology existed on the surface of SnS_2 microspheres. The excellent hydrophilicity of SnS_2 structure would endow this unique nano-canyon morphology with a powerful function (Figure 4A)—*capillary effect*—which can break the diffusion limit of molecules in aqueous solution.[39,40] When a droplet evaporated on the surface of substrates, the large amount of capillary attraction would guide most MeB molecules to enrich on the surface of SnS_2 microspheres. Initiated from these views, Raman mapping images with microscope regions of 72×48 μm^2 for 10^{-10} M MeB on SnS_2 microspheres were measured to provide more intuitive evidence for the enrichment phenomenon of probe molecules (Figures 4B and S9). Comparing the optical magnification picture and Raman mapping image from the same Raman measured area, it was found that when the concentration of MeB molecules decreased to 10^{-10} M, the enrichment phenomenon of MeB molecules started to emerge on the surface of SnS_2 microspheres. Moreover, this molecular enriching area presented an obvious ultra-high Raman intensity at 1,620 cm^{-1} (refer to the yellow and red areas in Figure 4B). As long as we were able to scan and detect the enriching area of low-concentrations molecules on SnS_2 microsphere substrates, the high-intensity Raman signal could be obtained. Therefore, the Raman detection of molecules with ultra-low concentration was achieved due to the *capillary effect* on the surface of SnS_2 microspheres, which endowed SnS_2 microspheres with ultra-low LOD that other pure semiconductor-based SERS substrates are unable to surpass. Additionally, benefiting from the unique nano-canyon morphology and capillary effect on the surface of SnS_2 microspheres, additional physical enrichment of molecules in the aqueous solution will be generated. As shown in Figure 4C, Raman spectra of immersing SnS_2 in the 10^{-7} M MeB solution and dropping 10^{-7} M MeB solution on SnS_2 were detected to

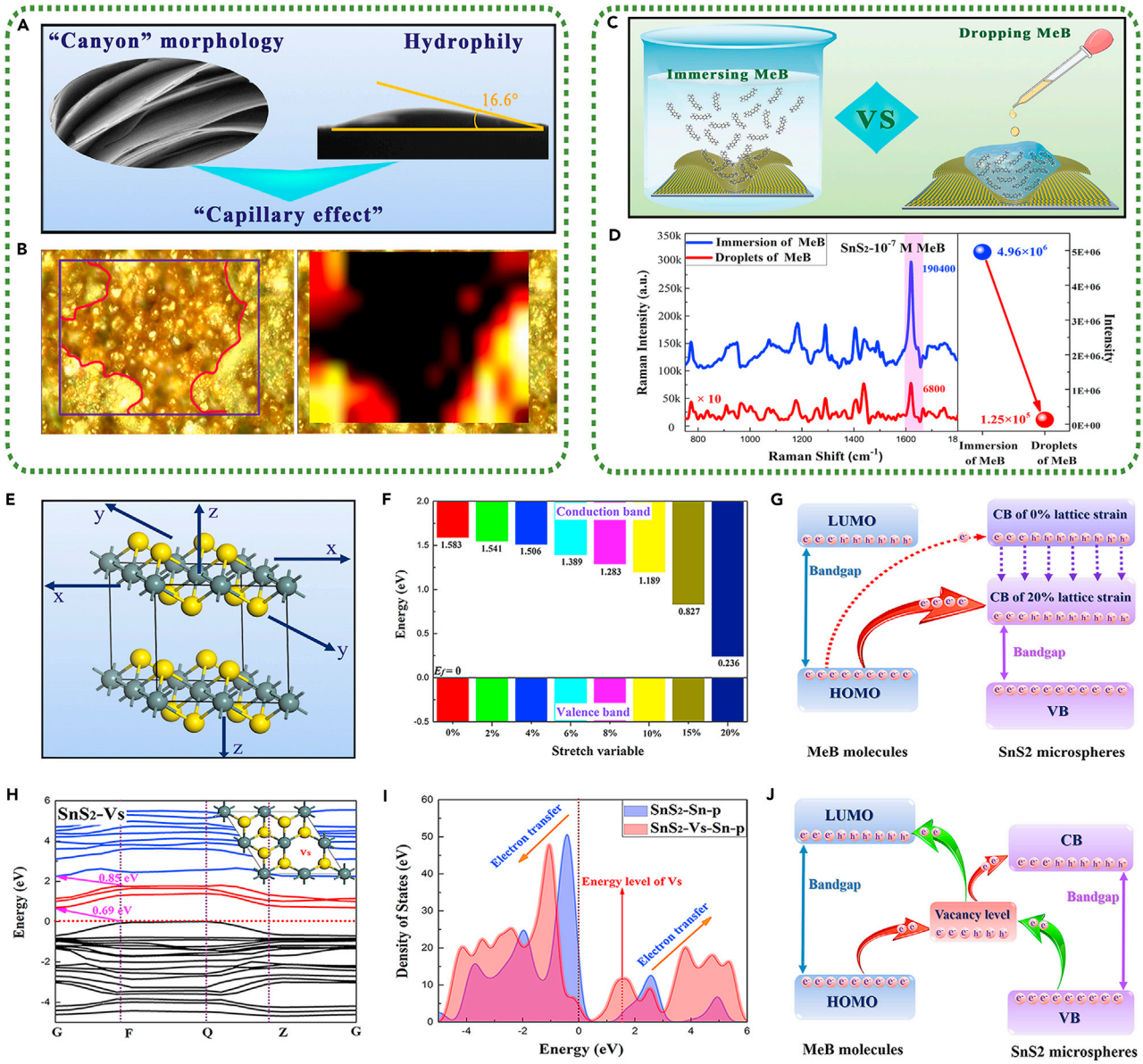

Figure 4. The proposed SERS enhancement mechanisms of *capillary effect*, lattice strain, and sulfur vacancies for SnS_2 microspheres

(A) Schematic diagram of combining *nano-canyon* morphology and hydrophilicity to induce the *capillary effect*.

(B) Raman mapping image with 72 × 48 μm^2 region of 10^{-10} M MeB on SnS_2 microspheres.

(C) Schematic diagram of immersing and dropping MeB molecules to explore physical enrichment.

(D) Raman spectra and SERS intensity of immersing and dropping 10^{-7} M MeB on SnS_2 microspheres.

(E) Schematic diagram of hexagonal SnS_2 crystal with the tensile strain in three periodic directions (x, y, and z axis).

(F) Bandgap of hexagonal SnS_2 crystal with 0%–20% tensile strain.

(G) Schematic diagram of charge transfers between MeB molecules and the hexagonal SnS_2 crystal with 0%–20% tensile strain.

(H) Band structure of SnS_2 crystal with sulfur vacancies.

(I) Density of states of Sn p orbitals in the perfect SnS_2 crystal and SnS_2 crystal with sulfur vacancies.

(J) Schematic diagram of charge transfers between MeB molecules and the hexagonal SnS_2 crystal with S vacancies.

explore the physical enrichment effect of SnS_2 microspheres substrates. Raman spectra in Figure 4D showed that the Raman intensity of immersing MeB molecules was far stronger than that of dropping MeB molecules. The calculating results indicated that SnS_2 microspheres could achieve about 40-fold physical enrichment for MeB molecules in

aqueous solution (SI-2 of the supplemental information), which could significantly improve the SERS sensitivity of substrates.

Recent research has demonstrated that the chemical mechanism (CM) contributed by charge transfer mainly governs the SERS-enhanced effect of two-dimensional (2D) semiconductor-based substrates. Therefore, in addition to the contribution of the capillary effect to SERS performance, it is necessary to consider the regulation of the electronic structure of hexagonal SnS_2 to the CM enhancement. Based on the analyzed results of XRD and HTREM, the hexagonal SnS_2 crystal exhibited lattice strain. Therefore, the lattice constants of the hexagonal SnS_2 crystal in the three periodic directions applying a tensile strain were changed to explore the influence of lattice strain on the electronic structure (Figure 4E). As shown in Figures 4F and S10, it was found that the bandgap decreased from 1.583 to 0.236 eV while increasing the tensile strain from 0% to 20%, which could be attributed to both electrons of Sn-p orbitals and S-s orbitals in the conduction band shifting to the Fermi level, although the energy of the valence band remained unchanged. The decreased energy level of the conduction band would stimulate the larger probability of charge transfer from the molecular HOMO to the conduction band of semiconductor-based substrates, thus significantly enhancing the chemical bond vibration of molecules[41] (Figure 4G). Additionally, the superficial defect states of SnS_2 microspheres could effectively break the restriction of the large bandgap on the charge transfer induced by the irradiation of visible light though introducing the intermediate energy level. As mentioned in the XPS results, sulfur vacancies (Vs) existed in the hexagonal SnS_2 crystal. Therefore, the SnS_2 crystal structure with sulfur vacancies was constructed, and the band structure and density of states are shown in Figures 4H, 4I, and S11. Compared with the electronic structure of the perfect hexagonal SnS_2 crystal, the defect energy levels between the conduction band and the Fermi level were introduced due to the existence of sulfur vacancies, thereby simultaneously making the electrons of the valence band shift to the deeper energy level and increasing the excited-state electrons of the conduction band.[27,28] The introduced defect energy levels served as an intermediate springboard for electronic transitions, which could further promote the charge transfers from the molecular HOMO to the conduction band of the semiconductor or the valence band of the semiconductor to the molecular LUMO (Figure 4J). In conclusion, the ultra-low SERS LOD of SnS_2 microspheres mainly contributed by the synergistic enhancements of the molecular enrichment caused by capillary effect and the charge transfer chemical enhancement boosted by the lattice strain and sulfur vacancies.

SERS detection of various SARS-CoV-2 biomarkers and establishing identification standard of SERS signals

With the COVID-19 pandemic that has swept the world, there has been an urgent solution needed for accurate identification of the infectiousness of SARS-CoV-2. It is well acknowledged that SARS-CoV-2 is an enveloped virus, and the viral surface mainly contains two transmembrane proteins: spike glycoprotein (S) and membrane protein (M), while the larger RNA genome is contained within the envelope[42] (Figure S12). Generally, the active or un-lysed coronavirus is covered by spike glycoprotein with a vertical size of about 5 nm. During the semiconductor-based SERS detection process, the SARS-CoV-2 S protein is the main contact with SnS_2 microsphere substrates, resulting in detectable characteristic Raman signals that usually contain the surface S protein dominating the SERS-Raman spectra of SARS-CoV-2.[16] After the SARS-CoV-2 is lysed and inactivated, its viral structure and spatial configuration are destroyed, and the nucleic acids (RNA) and other proteins originally wrapped in the envelope are exposed or released outside the virus

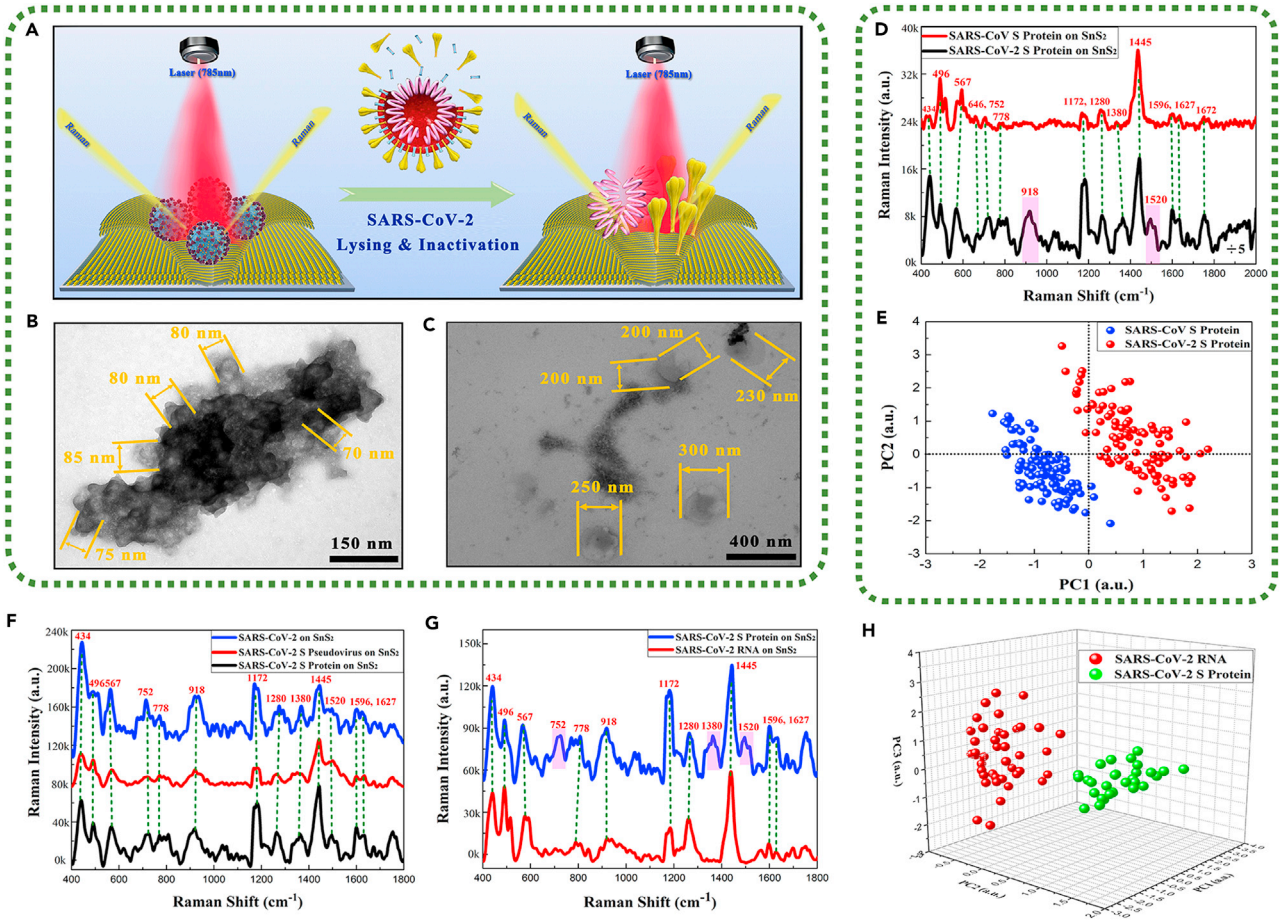

Figure 5. Application of SnS_2 microspheres for detecting various physical forms of SARS-CoV-2

(A) Schematic diagram of identifying the lysed SARS-CoV-2.

(B) TEM images of SARS-CoV-2 with complete viral structure.

(C) TEM images of the lysed SARS-CoV-2.

(D) Raman spectra of SARS-CoV-2 S protein and SARS-CoV S protein.

(E) The key features of SERS patterns to classify the SARS-CoV-2 S protein and SARS-CoV S protein.

(F) Raman spectra of physical forms of SARS-CoV-2 including SARS-CoV-2, SARS-CoV-2 S pseudovirus, and SARS-CoV-2 S protein.

(G) Raman spectra of SARS-CoV-2 RNA and SARS-CoV-2 S protein.

(H) The key features of SERS patterns to classify the RNA and S protein of SARS-CoV-2.

particle (Figure 5A). Therefore, the infectiousness of SARS-CoV-2 could be identified by analyzing the SERS signal difference in the surface S protein and internal RNA between the coronavirus with complete viral structure and the lysed coronavirus. First, the 120-kV scanning TEM was applied to observe the morphology of the SARS-CoV-2 with complete viral structure and the lysed SARS-CoV-2. The TEM images demonstrated typical intact virions with 70–120 nm size before lysing (Figures 5B and S13A) whereas enlarged and broken virions with about 200–300 nm size after lysing by ultrasound treatment are found (Figures 5C and S13B), suggesting the effective destruction of the integrity of SARS-CoV-2 particles by our lysing method.

We then characterized SERS spectra of five physical forms of SARS-CoV-2: SARS-CoV-2 S pseudovirus, SARS-CoV-2 S protein, SARS-CoV-2 RNA, lysed SARS-CoV-2, and SARS-CoV-2 (SI-5 of the supplemental information). The resultant Raman vibration modes corresponding to their Raman peaks are shown in Table S3. First, the interference of phosphate-buffered saline could be ignored due to its extremely weak Raman peaks in relation

to the Raman spectra of SARS-CoV-2 S pseudovirus (Figure S14). In order to confirm the accuracy of obtained Raman spectra for these various coronaviral physical forms on SnS_2 microspheres, Au nanoarrays were used as SERS substrates for reference (Figure S15). Analysis results indicated that Raman peaks of SARS-CoV-2 S pseudovirus, SARS-CoV-2 S protein, and SARS-CoV S protein on both substrates matched better with some Raman shifts due to the difference in SERS enhancement mechanisms and the amount of charge transfer between these two SERS substrates. The Raman spectra and the principal component analysis (PCA) results of S protein of SARS-CoV and SARS-CoV-2 (Figures 5D and 5E) both suggested that Raman peaks of these two kinds of S proteins could be completely distinguished in the 2D space, and the SARS-CoV-2 S proteins exhibited the characterized Raman bands at 918 cm^{-1} and 1,520 cm^{-1} corresponding to the vibration modes of C-C stretching in skeleton and N-H and C-O in-plane deformation in amide II. Although the S protein of SARS-CoV-2 and SARS-CoV showed up to 74.6% identity in their amino acid sequences (SI-4 of the supplemental information), SnS_2 microspheres still showed excellent identification ability for different biomolecules, which provided a promising SERS substrate candidate for practical detection applications of biomolecules. Additionally, three physical forms of SARS-CoV-2 including SARS-CoV-2, SARS-CoV-2 S pseudovirus, and SARS-CoV-2 S protein absorbing on SnS_2 microspheres presented almost identical Raman shifts except for the difference in Raman intensity (Figure 5F), which could be attributed to the fact that their main contact with SnS_2 microsphere substrates was the SARS-CoV-2 S protein, resulting in the same Raman peaks as SARS-CoV-2 S protein. Therefore, it is reasonable to replace the dangerous active SARS-CoV-2 with the SARS-CoV-2 S protein to obtain a large amount of Raman data for the principal component of machine learning analysis. Finally, the identification standard of SERS signals was established by machine learning and identification techniques to identify the non-infectious SARS-CoV-2. Raman spectra of SARS-CoV-2 RNA on SnS_2 microspheres were detected and are shown in Figures 5G and S16. Interestingly, PCA results in Figure 5H showed that SARS-CoV-2 RNA and S protein presented different Raman shifts, and they could be completely distinguished in the three-dimensional space. The SARS-CoV-2 S protein exhibited three characterized Raman bands at 752 cm^{-1}, 1,380 cm^{-1}, and 1,520 cm^{-1} originated from the vibration modes of the aromatic ring in tryptophan (Trp), C-N stretching in tryptophan (Trp), and N–H and C–O in-plane deformation in amide II, respectively. Therefore, Raman spectra of SARS-CoV-2 RNA and S protein could serve as two principal components of the identification standard to distinguish and classify the unknown SARS-CoV-2 samples. Similarly, the PCA results of SARS-CoV-2 were consistent with the SARS-CoV-2 S protein, showing the completely distinguished Raman peaks from SARS-CoV-2 RNA (Figure S17). Additionally, we further explored the limits of detection for three physical forms of SARS-CoV-2 virus based on SnS_2 microsphere SERS substrates. As shown in Figure S18, even if the SARS-CoV-2 S protein, SARS-CoV-2 RNA, and SARS-CoV-2 S pseudovirus were diluted to 10^{-14} mol/L, 10^4 copies/mL, and 10^4 copies/mL, respectively, some obvious, characteristic Raman signal of the above three physical forms of SARS-CoV-2 could still be detected by adsorbing on SnS_2 microspheres. To the best of our knowledge, it is the highest detection sensitivity for SARS-CoV-2 particles among the pure semiconductor-based SERS substrates, which also mainly originated from the molecular enrichment phenomenon caused by the capillary effect and the significant chemical enhancement of SnS_2 microspheres, but the difference is that virus particles are relatively less affected by capillary attraction due to their larger size. Moreover, the viral loads of SARS-CoV-2 identified from COVID-19 patients' saliva, stool, urine, or blood and the items in the cold chain environments were in the range of 10–10^{10} copies/mL, where the currently pandemic SARS-CoV-2 variants generally exhibit a characteristic of high viral load of >10^5 copies/mL.[3,43–49] Therefore, the SERS detection method based on SnS_2 microsphere substrates shows great practical application potential.

Diagnosis of the infectiousness of SARS-CoV-2 based on the established identification standard

Herein, the SARS-CoV-2 with complete viral structure and the lysed SARS-CoV-2 were adopted to simulate three contamination situations of SARS-CoV-2 in actual environments: the SARS-CoV-2 with complete viral structure, the lysed SARS-CoV-2, and a mixture of the complete-structure viruses and the lysed viruses. The experimental procedure for diagnosing the infectiousness of SARS-CoV-2 is shown in Figure 6A. Noticeably, the SARS-CoV-2 with complete viral structure showed only the characteristic Raman spectra of SARS-CoV-2 S protein (Figure S19A), whereas the lysed SARS-CoV-2 presented both the characteristic Raman peaks of SARS-CoV-2 S protein and RNA (Figure S19B). Based on the above identification standard of SERS signals for SARS-CoV-2 S protein and RNA, it is possible to complete the diagnosis of the non-infectious virus samples through two-step SERS detections. Multiple testing areas on the surface of SnS_2 substrates with these three virus samples were randomly selected to perform Raman detection to obtain at least 80 available SERS spectra, and a more advanced machine learning method of support vector machine (SVM) was adopted to discriminate and classify the obtained SERS spectra (Figure 6C). According to the first SERS detection results (Figures 6B, 6D, and 6F), if all the Raman spectra of virus sample belong to the SARS-CoV-2 S protein, this virus sample is determined to be the SARS-CoV-2 with complete viral structure, suggesting a severe risk of virus infectivity (Figure 6F). SVM analysis results of Figures 6B and 6D showed that 58 and 60 SERS spectra of virus samples could be correctly classified to SARS-CoV-2 RNA, while 71 and 26 SERS spectra could be contributed to SARS-CoV-2 S protein. Such SVM analysis results only indicated that there were some lysed SARS-CoV-2 virions in these two kinds of virus samples, but it could not judge their virus infectivity. Therefore, it is necessary to conduct the second SERS detection after eliminating RNA and re-lysing these two virus samples. Their SVM analysis results are shown in Figures 6E and 6G. If the virus sample still exhibits the characteristic Raman peaks of SARS-CoV-2 RNA at this time (Figures 6E and S20), it is diagnosed as the mixture of the complete-structure virus and the lysed virus, suggesting a moderate risk of virus infectivity. As shown in Figures 6G and S21, we found that 127 SERS spectra of the virus sample were all classified to SARS-CoV-2 S protein, indicating this virus sample belonged to the lysed SARS-CoV-2. Noticeably, this virus sample of all lysed SARS-CoV-2 in actual environments had almost no risk of virus infectivity, but it is frequently misdiagnosed as a source of infectious SARS-CoV-2 by the current commonly used detection method of RT-PCR. In conclusion, the present analysis results demonstrated that it is feasible to diagnose the non-infectious SARS-CoV-2 based on the identification standard of SERS signal for SARS-CoV-2 S protein and RNA, which paves a new path for the identification of SARS-CoV-2-contaminated dangerous items in actual environments.

Conclusions

In summary, in response to the challenge of diagnosing the infectiousness of SARS-CoV-2 in the various actual virus-contaminated environments, we developed ultrasensitive SERS substrate SnS_2 microspheres to detect various physical forms of SARS-CoV-2 virus. The first synthesized SnS_2 microspheres exhibited a hierarchical nanostructure with a unique *nano-canyon* morphology, which could generate *capillary effect* on the surface of microspheres. Based on these SnS_2 microsphere substrates, the Raman detection of molecules with ultra-low concentration was achieved through the molecular enrichment caused by capillary effect, which enabled SnS_2 microspheres to achieve about 40-fold physical enrichment for molecules. Additionally, benefiting from the contribution of the lattice strain and sulfur vacancies to chemical enhancement, SnS_2 microspheres exhibited an ultra-low

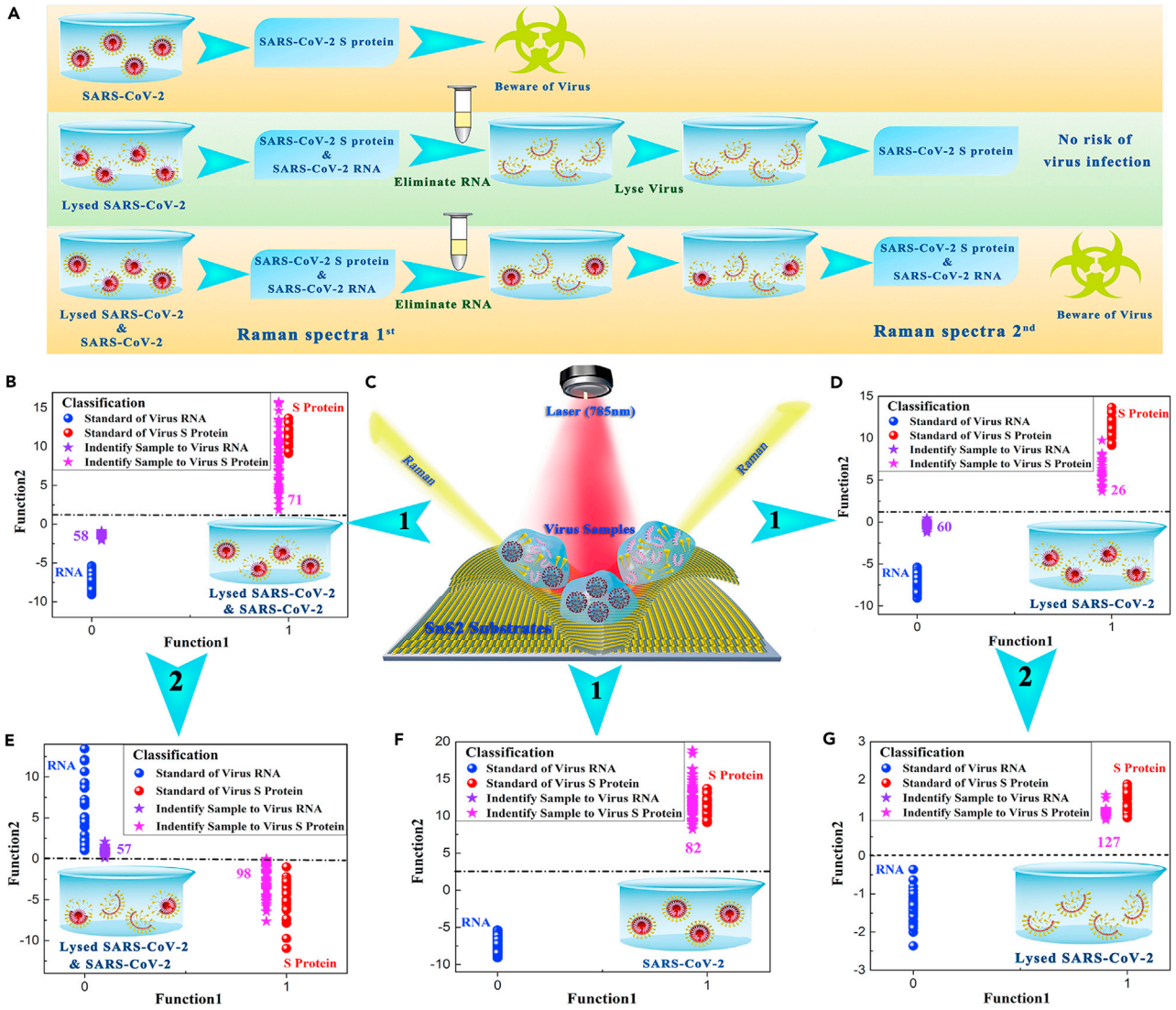

Figure 6. Application of SnS_2 microspheres for diagnosing the infectiousness of SARS-CoV-2

(A) Experimental procedure for diagnosing the infectiousness of SARS-CoV-2.

(B) SVM analysis results to identify the mixture of the SARS-CoV-2 with complete viral structure and the lysed SARS-CoV-2.

(C) Raman scattering diagram of three contamination situations of the novel coronavirus based on SnS_2 substrates.

(D) SVM analysis results to identify the lysed SARS-CoV-2.

(E) SVM analysis results to identify the mixture of the SARS-CoV-2 with complete viral structure and the lysed SARS-CoV-2 after eliminating RNA and re-lysing virus samples.

(F) SVM analysis results to identify the SARS-CoV-2 with complete viral structure.

(G) SVM analysis results to identify the lysed SARS-CoV-2 after eliminating RNA and re-lysing virus samples.

LOD of 10^{-13} M and an ultra-high enhancement factor of 3.0×10^8 for MeB. To the best of our knowledge, this remarkable SERS enhancement of SnS_2 microspheres is one of the highest sensitivities among the reported pure semiconductor-based SERS substrates, which can even parallel that of the noble metals with *hot spots*. As a result, various physical forms of SARS-CoV-2 were able to be sensitively detected on SnS_2 microspheres, and the identification standard of SARS-CoV-2 RNA and S protein was established by PCA methods. Moreover, based on the advanced machine learning method of SVM, non-infectious lysed SARS-CoV-2 was successfully distinguished, which paved a new path for identifying the infectiousness

of SARS-CoV-2 virions and is of significance to avoid misdiagnosing infectious SARS-CoV-2 in actual environments. Furthermore, it is worthwhile to note that recovery of SARS-CoV-2 in viral culture is currently the only approach to confirm the presence of replication-competent virus.[50] However, the viral culture method suffers from the defects of long culture time and complicated experimental operation. Meaningfully, the aforementioned two-step SERS detection method can be extended to rapidly diagnose SARS-CoV-2 infectivity on site in some contaminated patient gathering places such as hospitals or at the Centers for Disease Control and Prevention, exhibiting vital timeliness in patient management that the viral culture method does not have.

EXPERIMENTAL PROCEDURES

Resource availability

Lead contact

The detailed experimental methods can be found in the supplemental experimental procedures. It is recommended to contact the lead contact directly for further information and requests for resources and materials: Yong Yang (yangyong@mail.sic.ac.cn).

Materials availability

This study did not generate new unique reagents or there are restrictions to availability.

Data and code availability

All data associated with this study are made publicly available, including the calculation of enrichment multiples, enhancement factor calculations, theoretical results from the DFT calculations, and data analysis results of machine learning methods.

SUPPLEMENTAL INFORMATION

Supplemental information can be found online at https://doi.org/10.1016/j.matt.2021.11.028.

ACKNOWLEDGMENTS

This work is supported by the financial support of the National Natural Science Foundation of China (No. 52172167). And the authors also gratefully acknowledge financial support from the Key Research and Development Plan of Anhui Province (No. 202104a07020032).

AUTHOR CONTRIBUTIONS

Conceptualization, Y.S.P. and Y.Y.; methodology, Y.S.P., C.L.L., and X.Y.L.; formal analysis, Y.S.P., C.L.L., and J.J.L.; investigation, Y.S.P, Y.Y.L., and J.W.; resources, Y.G., J.W., and J.H.; writing – original draft, Y.S.P.; writing – review & editing, Y.S.P., Y.Y., J.W., and J.H.; visualization, Y.S.P. and C.L.L.; supervision, Y.Y. and Z.R.H.; funding acquisition, Y.Y., Y.G., and J.H.

DECLARATION OF INTERESTS

The authors declare no competing interests.

Received: September 5, 2021
Revised: October 22, 2021
Accepted: November 25, 2021
Published: December 20, 2021

REFERENCES

1. Tang, Z.M., Kong, N., Zhang, X.C., Liu, Y., Hu, P., Mou, S., Liljeström, P., Shi, J.L., Farokhzad, O.C., Tao, W., et al. (2020). A materials-science perspective on tackling COVID-19. Nat. Rev. Mater. *5*, 847–860.
2. Tang, Z.M., Zhang, X.C., Shu, Y.Q., Guo, M., Zhang, H., and Tao, W. (2021). Insights from nanotechnology in COVID-19 treatment. Nano Today *36*, 101019.
3. Zhang, J., Fang, X., Mao, Y., Qi, H.C., Wu, J., Liu, X.R., You, F.S., Zhao, W.C., Chen, Y., and Zheng, L. (2021). Real-time, selective, and low-cost detection of trace level SARS-CoV-2 spike-protein for cold-chain food quarantine. NPJ Sci. Food *5*, 12.
4. Chi, Y.H., Wang, Q.X., Chen, G.S., and Zheng, S.L. (2021). The long-term presence of SARS-CoV-2 on cold-chain food packaging surfaces indicates a new COVID-19 winter outbreak: a mini review. Front. Public Health *9*, 650493.
5. Zou, L.R., Ruan, F., Huang, M.X., Liang, L.J., Huang, H.T., Hong, Z.S., Yu, J.X., Kang, M., Song, Y.C., Wu, J., et al. (2020). SARS-CoV-2 viral load in upper respiratory specimens of infected patients. N. Engl. J. Med. *382*, 1177–1179.
6. Zou, Y.Y., Uspal, W.E., and Tao, W. (2020). Airborne transmission of COVID-19: aerosol dispersion, lung deposition, and virus-receptor interactions. ACS Nano *14*, 16502–16524.
7. Halvorson, R.A., and Vikesland, P.J. (2010). Surface-enhanced Raman spectroscopy (SERS) for environmental analyses. Environ. Sci. Technol. *44*, 7749–7755.
8. Zhang, C., Li, C.H., Yu, J., Jiang, S.Z., Xu, S.C., Yang, C., Liu, Y.J., Gao, X.G., Liu, A.H., and Man, B.Y. (2018). SERS activated platform with three-dimensional hot spots and tunable nanometer gap. Sens. Actuators B *258*, 163–171.
9. Li, J.F., Panneerselvam, R., and Tian, Z.Q. (2010). Shell-isolated nanoparticle-enhanced Raman spectroscopy. Nature *464*, 392–395.
10. Zong, C., Xu, M.X., Xu, L.J., Wei, T., Ma, X., Zheng, X.S., Hu, R., and Ren, B. (2018). Surface-enhanced Raman spectroscopy for bioanalysis: reliability and challenges. Chem. Rev. *118*, 4946–4980.
11. Eom, G., Hwang, A., Kim, H., Yang, S., Lee, D.K., Song, S., Ha, K., Jeong, J., Jung, J., and Lim, E.K. (2019). Diagnosis of Tamiflu-resistant influenza virus in human nasal fluid and saliva using surface-enhanced Raman scattering. ACS Sens. *4*, 2282–2287.
12. Zhang, X.G., Zhang, X.L., Luo, C.L., Liu, Z.Q., Chen, Y.Y., Dong, S.L., Jiang, C.Z., Yang, S.K., Wang, F.B., and Xiao, X.H. (2019). Volume-enhanced Raman scattering detection of viruses. Small *15*, 1805516.
13. Shao, F., Lu, Z.C., Liu, C., Han, H.Y., Chen, K., Li, W.T., He, Q.G., Peng, H., and Chen, J.N. (2014). Hierarchical nanogaps within bioscaffold arrays as a high-performance SERS substrate for animal virus biosensing. ACS Appl. Mater. Interfcaes *6*, 6281–6289.
14. Li, Z.H., Leustean, L., Inci, F., Zheng, M., Demirci, U., and Wang, S.Q. (2019). Plasmonic-based platforms for diagnosis of infectious diseases at the point-of-care. Biotechnol. Adv. *37*, 107440.
15. Yeh, Y.T., Gulino, K., Zhang, Y.H., Sabestien, A., Chou, T.W., Zhou, B., Lin, Z., Albert, I., Lu, H.G., Swaminathan, V., et al. (2020). A rapid and label-free platform for virus capture and identification from clinical samples. PNAS *117*, 895–901.
16. Yang, Y., Peng, Y.S., Lin, C.L., Long, L., Hu, J.Y., He, J., Huang, Z.R., Li, Z.Y., Lombardi, J.R., Luo, X.Y., et al. (2021). Human ACE2-functionalized gold "virus-trap" nanostructures for accurate capture of SARS-CoV-2 and single-virus SERS detection. Nano-micro Lett. *13*, 109.
17. Chen, H., Park, S.G., Choi, N., Kwon, H.J., Kang, T., Lee, M.K., and Choo, J. (2021). Sensitive detection of SARS-CoV-2 using a SERS-based aptasensor. ACS Sens. *6*, 2378–2385.
18. Pramanik, A., Gao, Y., Patibandla, S., Mitra, D., McCandless, M.G., Fassero, L.A., Gates, K., Tandon, R., and Ray, P.C. (2021). The rapid diagnosis and effective inhibition of coronavirus using spike antibody attached gold nanoparticles. Nanoscale Adv. *3*, 1588–1596.
19. Peng, Y.S., Lin, C.L., Long, L., Masaki, T., Tang, M., Yang, L.L., Liu, J.J., Huang, Z.R., Li, Z.Y., Yang, Y., et al. (2021). Charge-transfer resonance and electromagnetic enhancement synergistically enabling MXenes with excellent SERS sensitivity for SARS-CoV-2 S protein detection. Nano-micro Lett. *13*, 52.
20. Lin, J., Ren, W.Z., Li, A.R., Yao, C.Y., Chen, T.X., Ma, X.H., Wang, X.T., and Wu, A.G. (2020). Crystal–amorphous core–shell structure synergistically enabling TiO_2 nanoparticles remarkable SERS sensitivity for cancer cell imaging. ACS Appl. Mater. Interfaces *12*, 4204–4211.
21. Yu, H.K., Peng, Y.S., Yang, Y., and Li, Z.Y. (2019). Plasmon-enhanced light-matter interactions and applications. NPJ Comput. Mater. *5*, 45.
22. Seo, J., Lee, J., Kim, Y., Koo, D., Lee, G., and Park, H. (2020). Ultrasensitive plasmon-free surface-enhanced Raman spectroscopy with femtomolar detection limit from 2D van der Waals heterostructure. Nano Lett. *20*, 1620–1630.
23. Yang, L.L., Peng, Y.S., Yang, Y., Liu, J.J., Huang, H.L., Yu, B.H., Zhao, J.M., Lu, Y.L., Huang, Z.R., Li, Z.Y., and Lombardi, J.R. (2019). A novel ultra-sensitive semiconductor SERS substrate boosted by the coupled resonance effect. Adv. Sci. *6*, 1900310.
24. Lombardi, J.R. (2017). Enhanced by organic surfaces. Nat. Mater. *16*, 878–880.
25. Shan, Y.F., Zheng, Z.H., Liu, J.J., Yang, Y., Li, Z.Y., Huang, Z.R., and Jiang, D.L. (2017). Niobium pentoxide: a promising surface-enhanced Raman scattering active semiconductor substrate. NPJ Comput. Mater. *11*, 3.
26. Zheng, Z.H., Cong, S., Gong, W.B., Xuan, J.N., Li, G.H., Lu, W.B., Geng, F.X., and Zhao, Z.G. (2017). Semiconductor SERS enhancement enabled by oxygen incorporation. Nat. Commun. *8*, 1993.
27. Cong, S., Yuan, Y.Y., Chen, Z.G., Hou, J.Y., Yang, M., Su, Y.L., Zhang, Y.Y., Li, L., Li, Q.W., Geng, F.X., and Zhao, Z.G. (2015). Noble metal-comparable SERS enhancement from semiconducting metal oxides by making oxygen vacancies. Nat. Commun. *6*, 7800.
28. Lin, J., Shang, Y., Li, X.X., Yu, J., Wang, X.T., and Guo, L. (2017). Ultrasensitive SERS detection by defect engineering on single Cu_2O superstructure particle. Adv. Mater. *29*, 1604797.
29. Guo, S.Y., Zhang, Y.P., Ge, Y.Q., Zhang, S.L., Zeng, H.B., and Zhang, H. (2019). 2D V-V binary materials: status and challenges. Adv. Mater. *39*, 1902352.
30. Quan, Y.N., Yao, J.C., Sun, Y.S., Qu, X., Su, R., Hu, M.Y., Chen, L., Liu, Y., Gao, M., and Yang, J.H. (2021). Enhanced semiconductor charge-transfer resonance: unprecedented oxygen bidirectional strategy. Sens. Actuators B *327*, 128903.
31. Wang, X.T., Shi, W.X., Wang, S.X., Zhao, H.W., Lin, J., Yang, Z., Chen, M., and Guo, L. (2019). Two-dimensional amorphous TiO_2 nanosheets enabling high-efficiency photoinduced charge transfer for excellent SERS activity. J. Am. Chem. Soc. *141*, 5856–5862.
32. Zhang, D.Z., Xu, Z.Y., Yang, Z.M., and Song, X.S. (2020). High-performance flexible self-powered tin disulfide nanoflowers/reduced graphene oxide nanohybrid-based humidity sensor driven by triboelectric nanogenerator. Nano Energy *67*, 104251.
33. Gong, Y.J., Yuan, H.T., Wu, C.L., Tang, P.Z., Yang, S.Z., Yang, A.K., Li, G.D., Liu, B.F., Van de Groep, J., Cui, Y., et al. (2018). Spatially controlled doping of two-dimensional SnS_2 through intercalation for electronics. Nat. Nanotechnol. *13*, 294–299.
34. Kitadai, H., Wang, X.Z., Mao, N.N., Huang, S.X., and Ling, X. (2019). Enhanced Raman scattering on nine 2D van der Waals materials. J. Phys. Chem. Lett. *10*, 3043–3050.
35. Zhang, M.M., Li, X.Y., Fan, S.Y., Yin, Z.F., Li, J.N., Zeng, L.B., Tade, M.O., and Liu, S.M. (2020). Novel two-dimensional $AgInS_2/SnS_2$/RGO dual heterojunctions: high spatial charge and toxicity evaluation. Langmuir *36*, 9709–9718.
36. Mondal, C., Ganguly, M., Pal, J., Roy, A., Jana, J., and Pal, T. (2014). Morphology controlled synthesis of SnS_2 nanomaterial for promoting photocatalytic reduction of aqueous Cr(VI) under visible light. Langmuir *30*, 4157–4164.
37. Lee, C.G., Yan, H.G., Brus, L.E., Heinz, T.F., Hone, J., and Ryu, S. (2010). Anomalous lattice vibrations of single- and few-layer MoS_2. ACS Nano *4*, 2695–2700.
38. Li, X.H., Guo, S.H., Su, J., Ren, X.G., and Fang, Z.Y. (2020). Efficient Raman enhancement in molybdenum disulfide by tuning the interlayer spacing. ACS Appl. Mater. Interfaces *12*, 28474–28483.
39. Guo, H., Qian, K., Cai, A.J., Tang, J., and Liu, J. (2019). Ordered gold nanoparticle arrays on

the tip of silver wrinkled structures for single molecule detection. Sens. Actuators B *300*, 126846.

40. Park, S.G., Mun, C., Xiao, X.F., Braun, A., Kim, S., Giannini, V., Maier, S.A., and Kim, D.H. (2017). Surface energy-controlled SERS substrates for molecular concentration at plasmonic nanogaps. Adv. Funct. Mater. *27*, 1703376.

41. Wang, X.T., Shi, W.X., Jin, Z., Huang, W.F., Lin, J., Ma, G.S., Li, S.Z., and Guo, L. (2017). Remarkable SERS activity observed from amorphous ZnO nanocages. Angew. Chem. Int. Ed. *33*, 9983–9987.

42. Wrapp, D., Wang, N.S., Corbett, K.S., Goldsmith, J.A., Hsieh, C.L., Abiona, O., Graham, B.S., and McLellan, J.S. (2020). Cryo-EM structure of the 2019-nCoV spike in the prefusion conformation. Science *367*, 1260–1263.

43. Zhang, Z.Y., Tang, Z.M., Farokhzad, N., Chen, T.F., and Tao, W. (2020). Sensitive, rapid, low-cost, and multiplexed COVID-19 monitoring by the wireless telemedicine platform. Matter *3*, 1818–1820.

44. Zheng, S.F., Fan, J., Yu, F., Feng, B.H., Lou, B., Zou, Q.D., Xie, G.L., Lin, S., Wang, R.N., Yang, X.Z., et al. (2020). Viral load dynamics and disease severity in patients infected with SARS-CoV-2 in Zhejiang province, China, January-March 2020: retrospective cohort study. BMJ *369*, m1443.

45. Peng, L., Liu, J., Xu, W.X., Luo, Q.M., Chen, D.B., Lei, Z.Y., Huang, Z.L., Li, X.J., Deng, K.J., Lin, B.L., and Gao, Z.L. (2020). SARS-CoV-2 can be detected in urine, blood, anal swabs, and oropharyngeal swabs specimens. J. Med. Virol. *92*, 1676–1680.

46. Pan, Y., Zhang, D., Yang, P., Poon, L.L., and Wang, M.Q. (2020). Viral load of SARS-CoV-2 in clinical samples. Lancet Infect. Dis. *20*, 411–412.

47. Yuan, X., Yang, C.M., He, Q., Chen, J.H., Yu, D.M., Li, J., Zhai, S.Y., Qin, Z.F., Du, K., Chu, Z.H., and Qin, P.W. (2020). Current and perspective diagnostic techniques for COVID-19. ACS Infect. Dis. *6*, 1998–2016.

48. Dai, M., Li, H.N., Yan, N., Huang, J.Y., Zhao, L., Xu, S.Q., Wu, J.M., Jiang, S.B., Pan, C.G., and Liao, M. (2021). Long-term survival of SARS-CoV-2 on salmon as a source for international transmission. J. Infect. Dis. *223*, 537–539.

49. Liu, H., Fei, C.N., Chen, Y.L., Luo, S.M., Yang, T., Yang, L., Liu, J., Ji, X.Y., Wu, W.S., and Song, J. (2021). Investigating SARS-CoV-2 persistent contamination in different indoor environments. Environ. Res. *202*, 111763.

50. Binnicker, M.J. (2021). Can testing predict SARS-CoV-2 infectivity? The potential for certain methods to be surrogates for replication-competent virus. J. Clin. Microbiol. *59*, e00469-21.

Matter, Volume *5*

Supplemental information

Identifying infectiousness of SARS-CoV-2 by ultra-sensitive SnS_2 SERS biosensors with capillary effect

Yusi Peng, Chenglong Lin, Yanyan Li, Yong Gao, Jing Wang, Jun He, Zhengren Huang, Jianjun Liu, Xiaoying Luo, and Yong Yang

Supplemental Information

I-Supplemental Figures and Notes

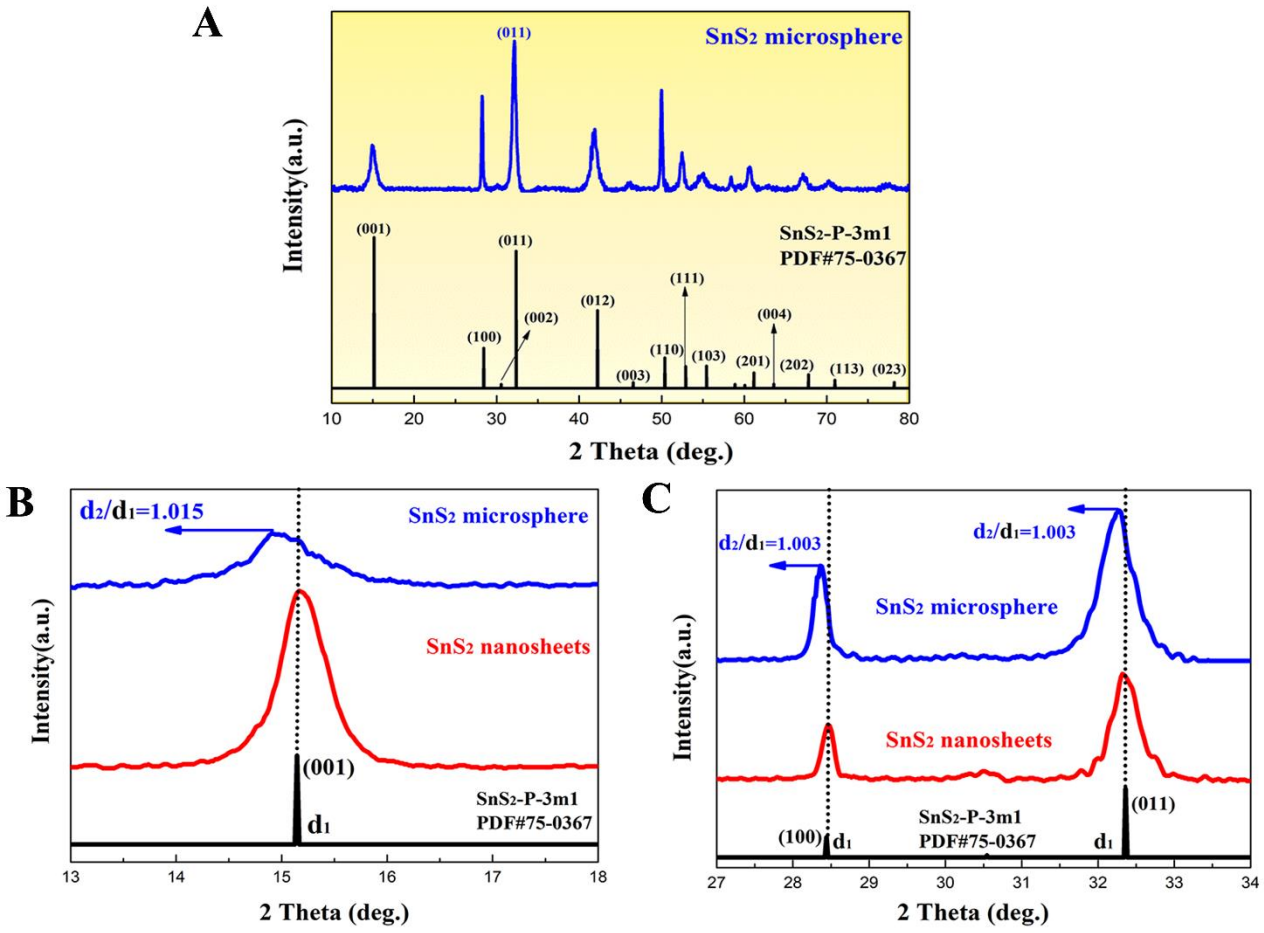

Figure S1. XRD characterization of SnS_2 microspheres.

(A) XRD pattern of SnS_2 microspheres.

(B, C) XRD pattern of SnS_2 microspheres and SnS_2 nanosheets with 2θ angle of 13°-18° and 27°-34°.

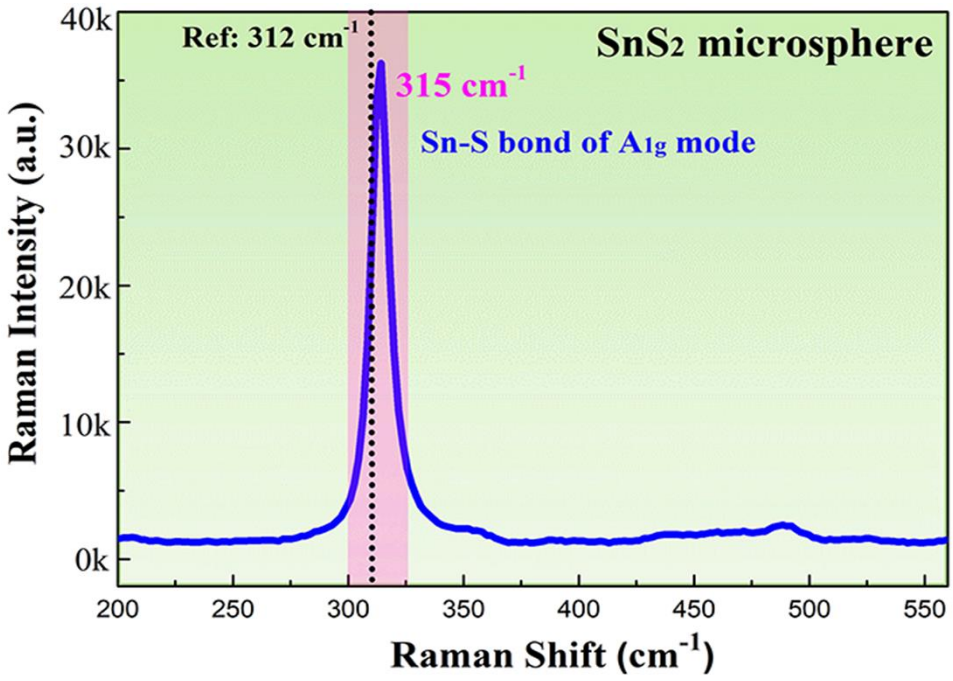

Figure S2. Raman spectra of SnS_2 microspheres.

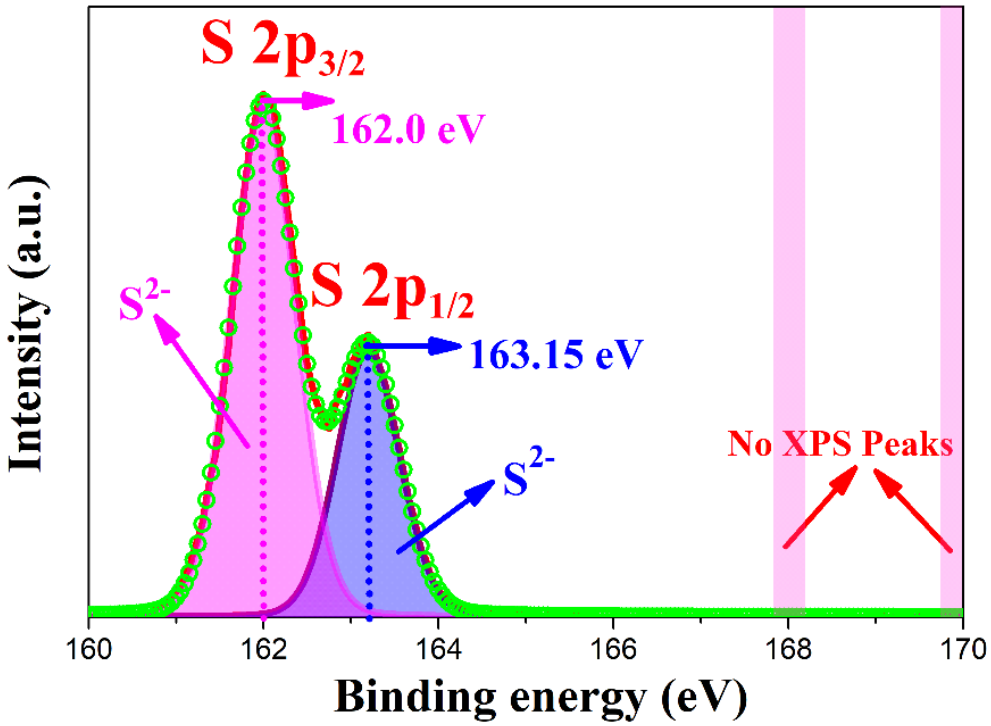

Figure S3. S2*p* XPS spectrum ranging from 160 eV to 170 eV of SnS_2 microspheres.

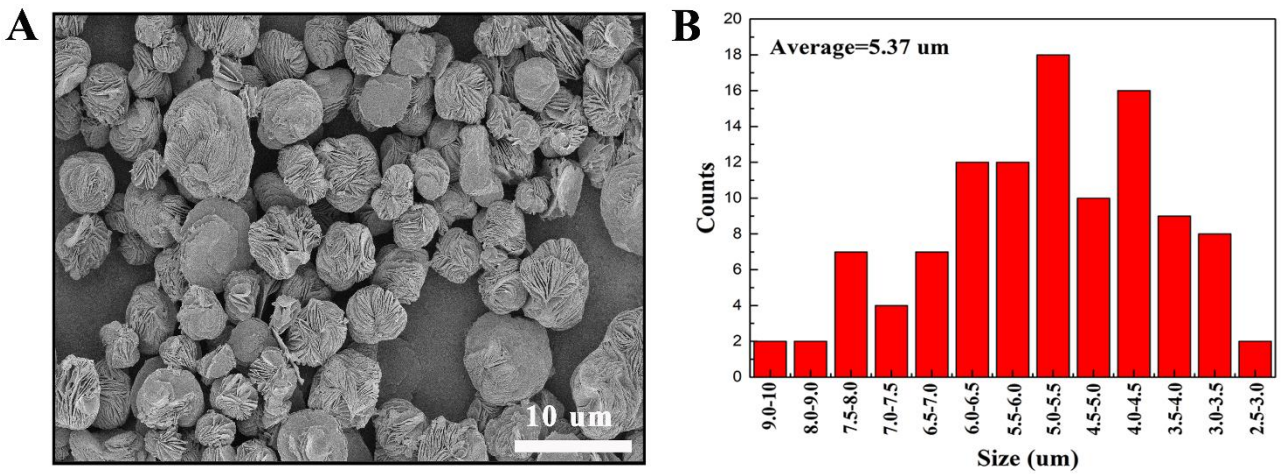

Figure S4. Morphology characterization of SnS_2 microspheres.

(A) The low-magnification SEM image of SnS_2 microspheres.

(B) The statistical size of SnS_2 microspheres.

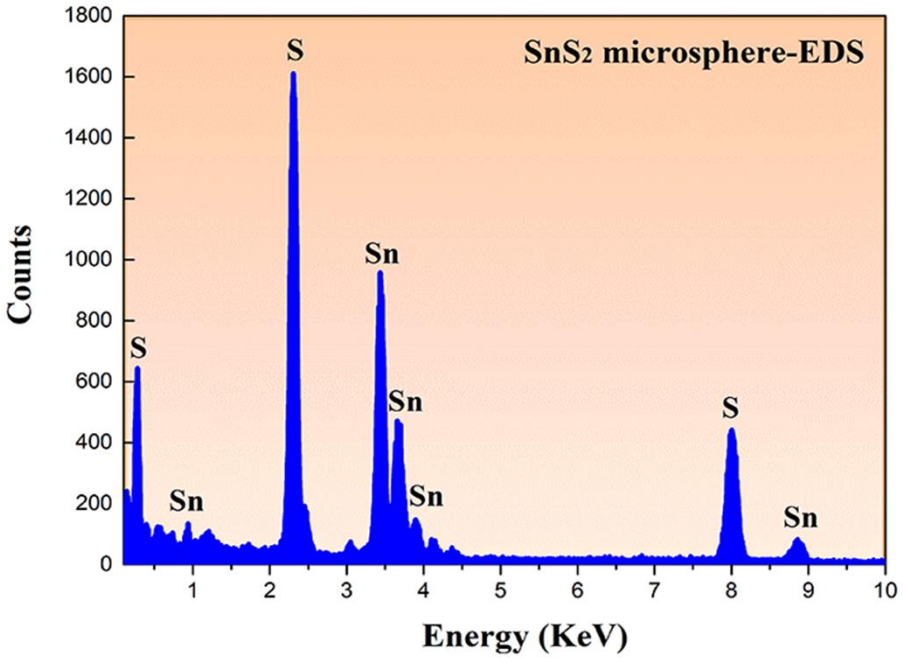

Figure S5. EDS spectrum of SnS_2 microspheres.

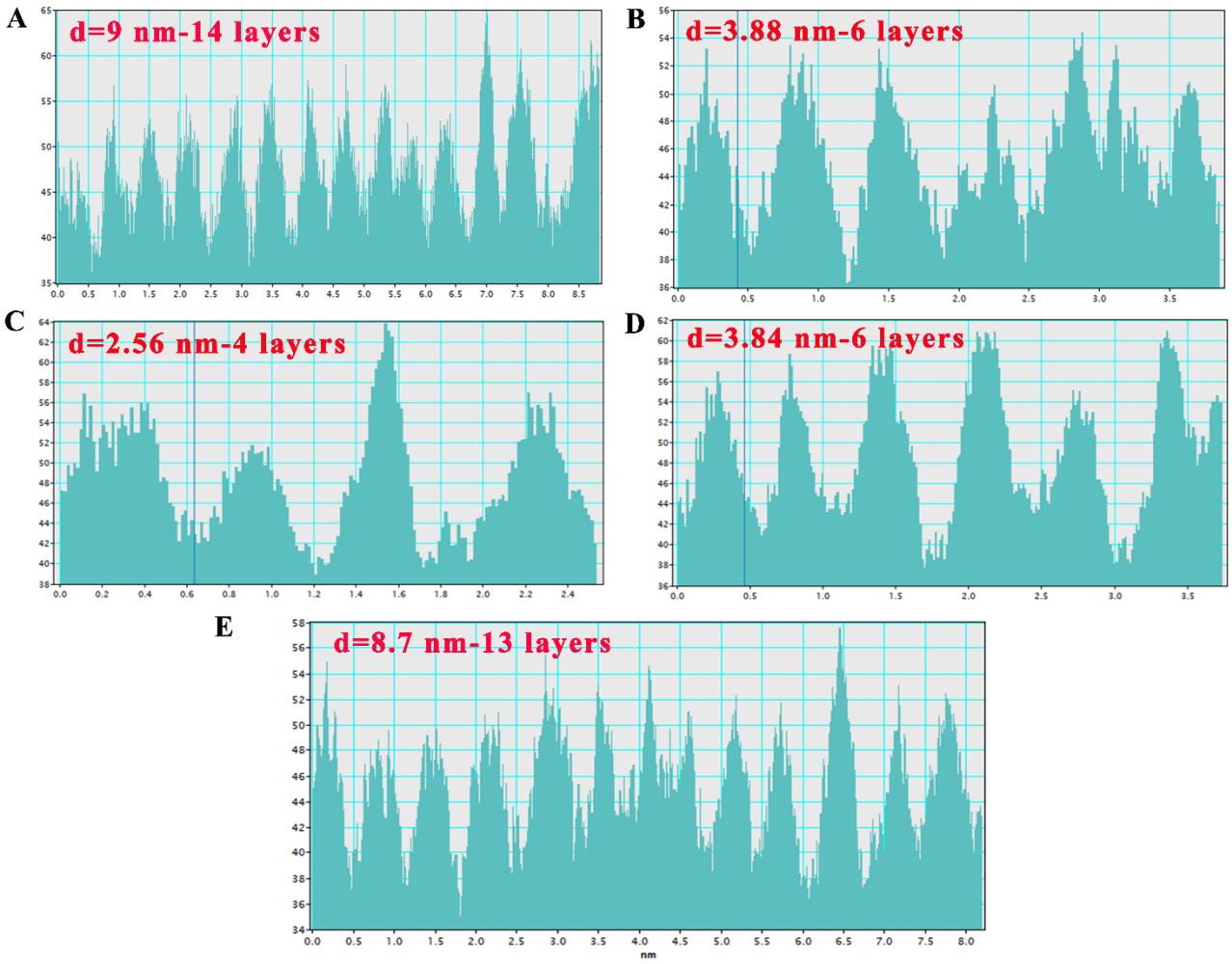

Figure S6. The evidence of lattice fringe space.

(A-E) The lattice fringe space of HRTEM images in Figure 2G for SnS_2 microspheres.

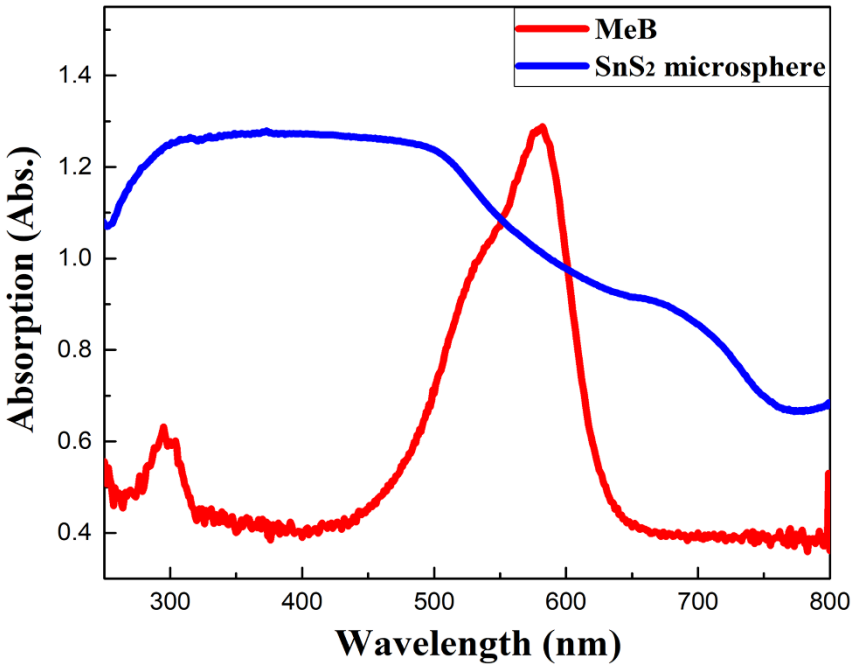

Figure S7. UV-vis optical absorption spectrum of SnS_2 microspheres and MeB molecules.

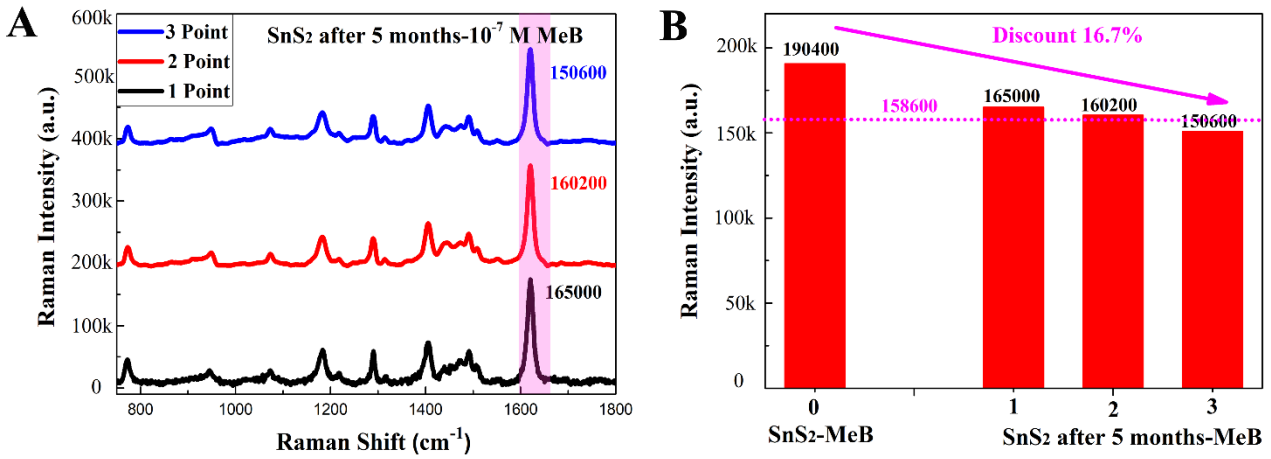

Figure S8. The SERS-enhanced stability of SnS_2 microsphere.

(A) Raman spectra of 10^{-7} M MeB on SnS_2 microsphere after 5 months.

(B) Comparison of Raman intensity for MeB molecules on fresh SnS_2 microsphere and SnS_2 microsphere after 5 months

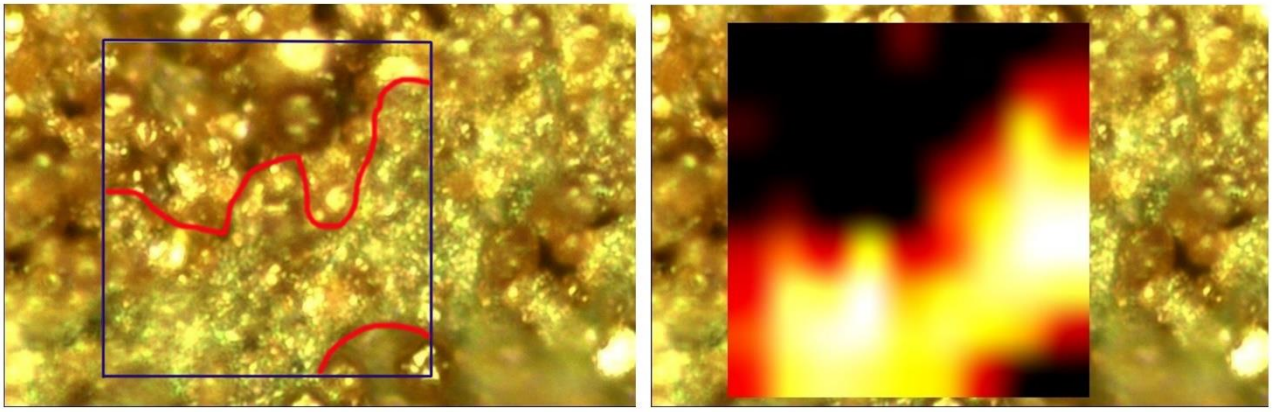

Figure S9. Raman mapping images with 72×48 μm^2 region of 10^{-10} M MeB on SnS_2 microspheres.

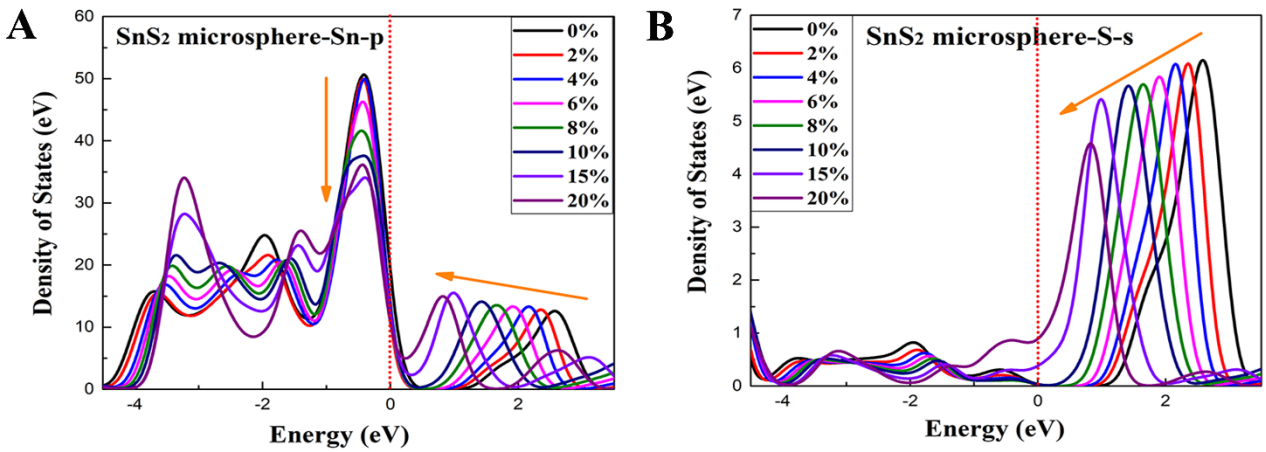

Figure S10. The electronic structure of SnS_2 crystal with tensile strain based on DFT calculations.

(A) Density of states of Sn-p orbitals in the hexagonal SnS_2 crystal with 0%-20% tensile strain.

(B) Density of states of S-s orbitals in the hexagonal SnS_2 crystal with 0%-20% tensile strain.

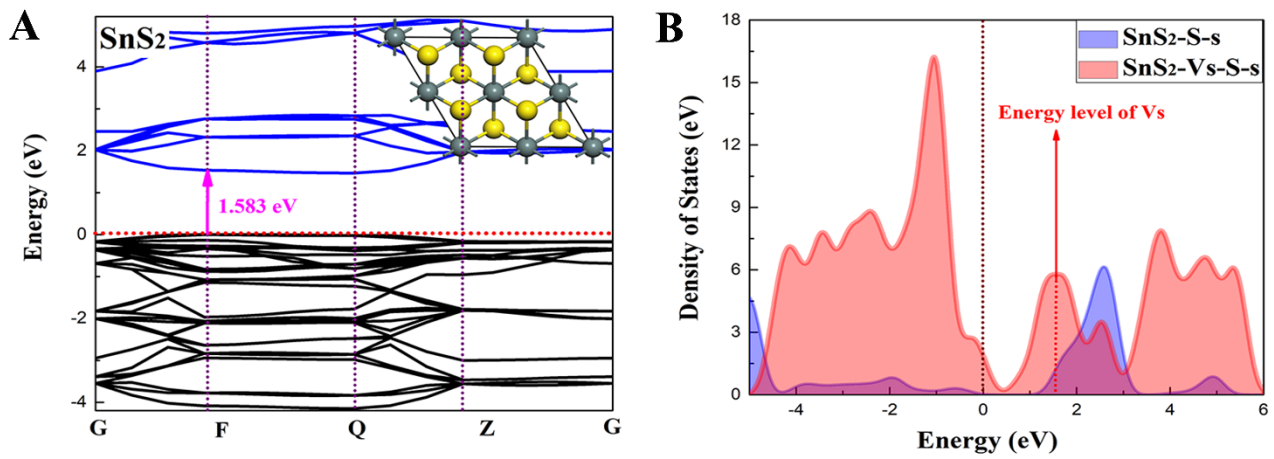

Figure S11. The electronic structure of SnS_2 crystal with sulfur vacancies based on DFT calculations.

(A) Band structure of the hexagonal SnS_2 crystal.

(B) Density of states of S s orbitals in the hexagonal SnS_2 crystal with sulfur vacancies.

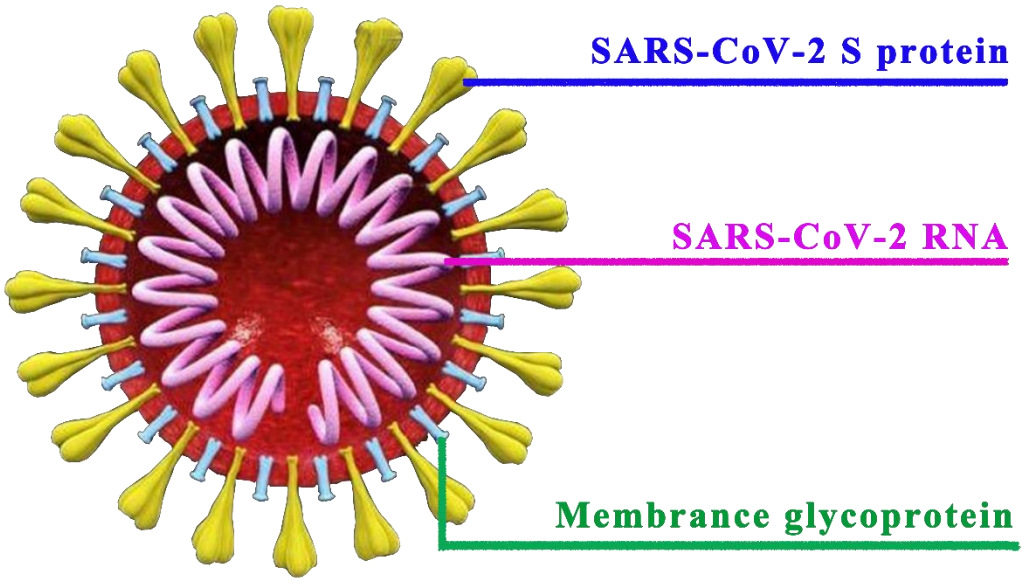

Figure S12. Schematic diagram of composition and structure for SARS-CoV-2.

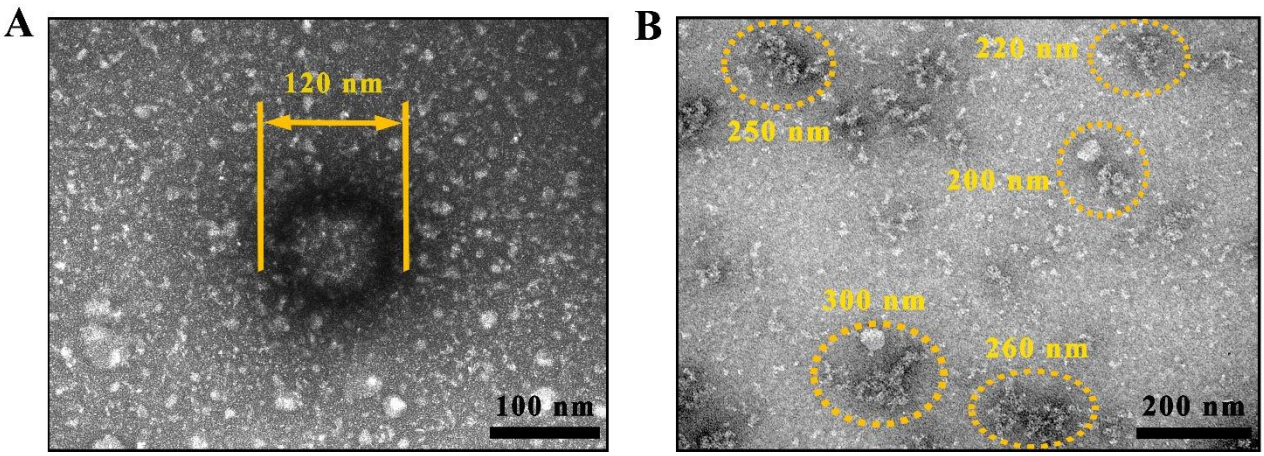

Figure S13. TEM characterization of SARS-CoV-2 viral structure.

(A) TEM images of SARS-CoV-2 with complete viral structure.

(B) TEM images of lysed SARS-CoV-2. The white agglomerates in TEM images are some protein impurities.

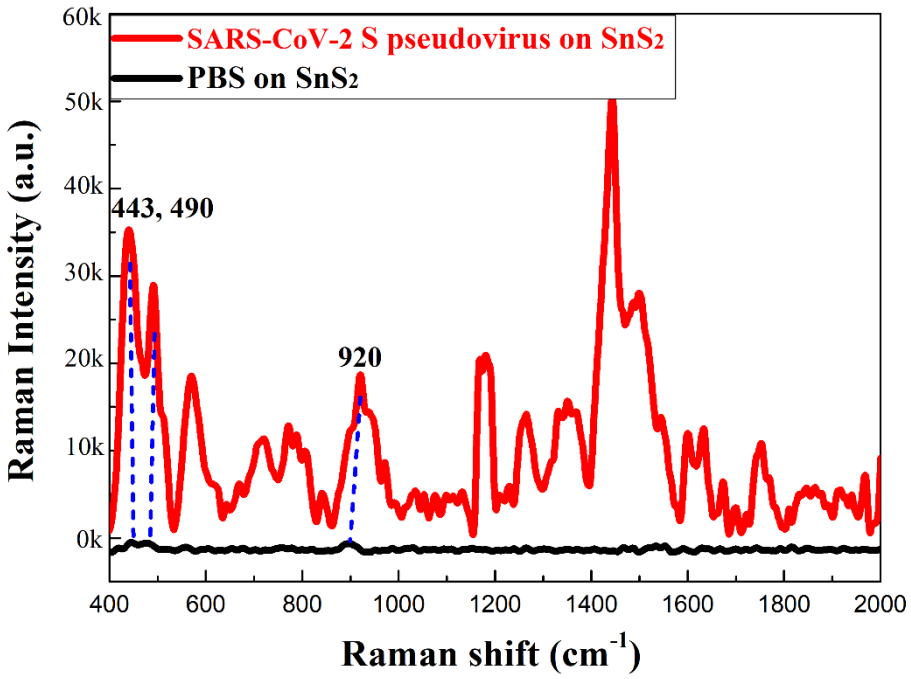

Figure S14. Raman spectra of SARS-CoV-2 S pseudovirus and PBS on SnS_2 microspheres.

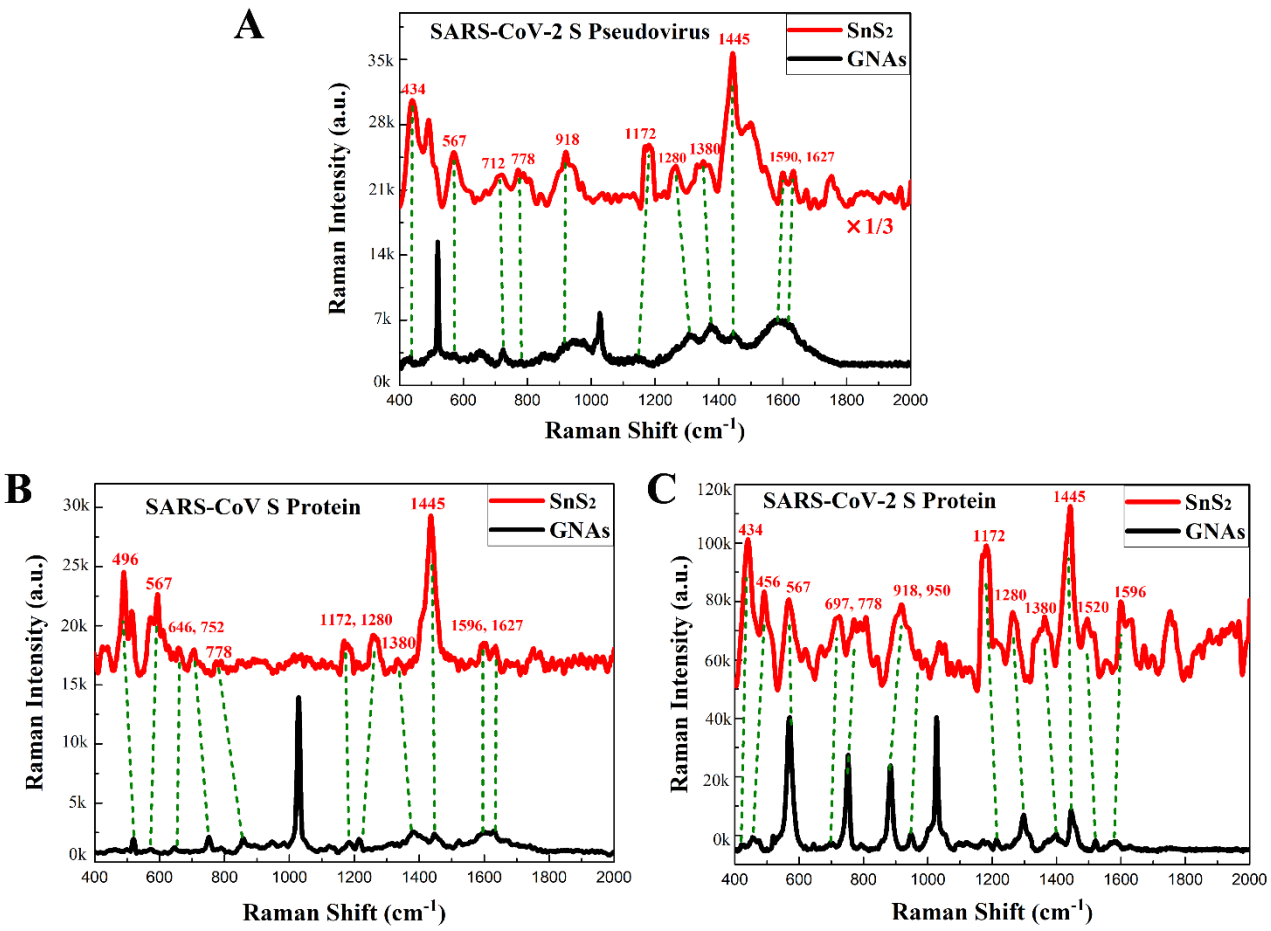

Figure S15. The accuracy research of viral Raman spectra.

(A) Raman spectra of SARS-CoV-2 S pseudovirus on SnS_2 microspheres and Au substrates.

(B) Raman spectra of SARS-CoV S protein on SnS_2 microspheres and Au substrates.

(C) Raman spectra of SARS-CoV-2 S protein on SnS_2 microspheres and Au substrates.

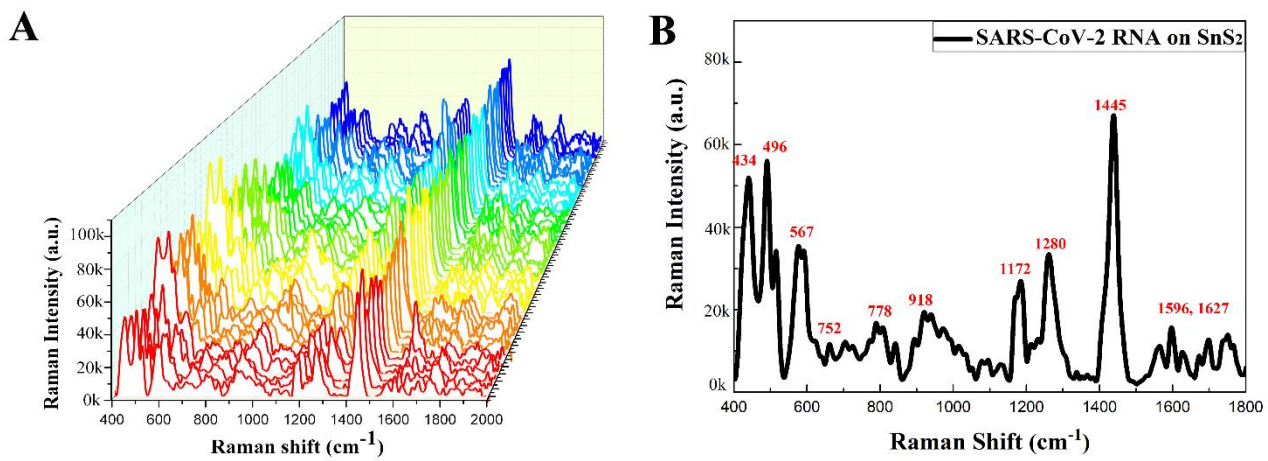

Figure S16. Raman spectra of SARS-CoV-2 RNA.

(A) Raman spectra of 46 measured points for SARS-CoV-2 RNA on SnS_2 microspheres.

(B) Raman spectra of SARS-CoV-2 RNA.

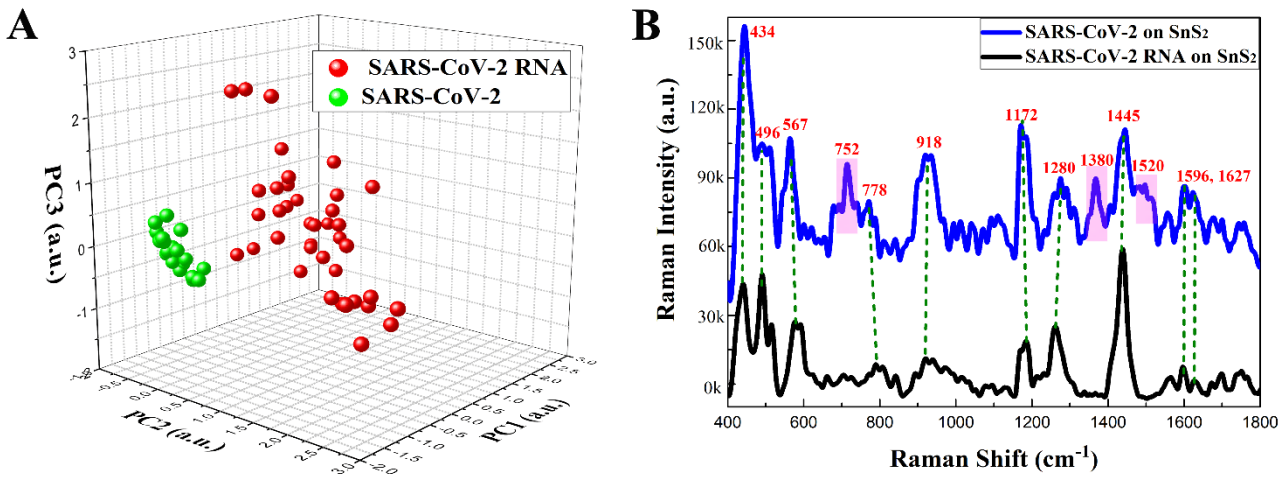

Figure S17. PCA and Raman peaks analysis of SARS-CoV-2 RNA and SARS-CoV-2.

(A) The key features of SERS patterns to classify the SARS-CoV-2 RNA and SARS-CoV-2.

(B) Raman spectra of SARS-CoV-2 RNA and SARS-CoV-2.

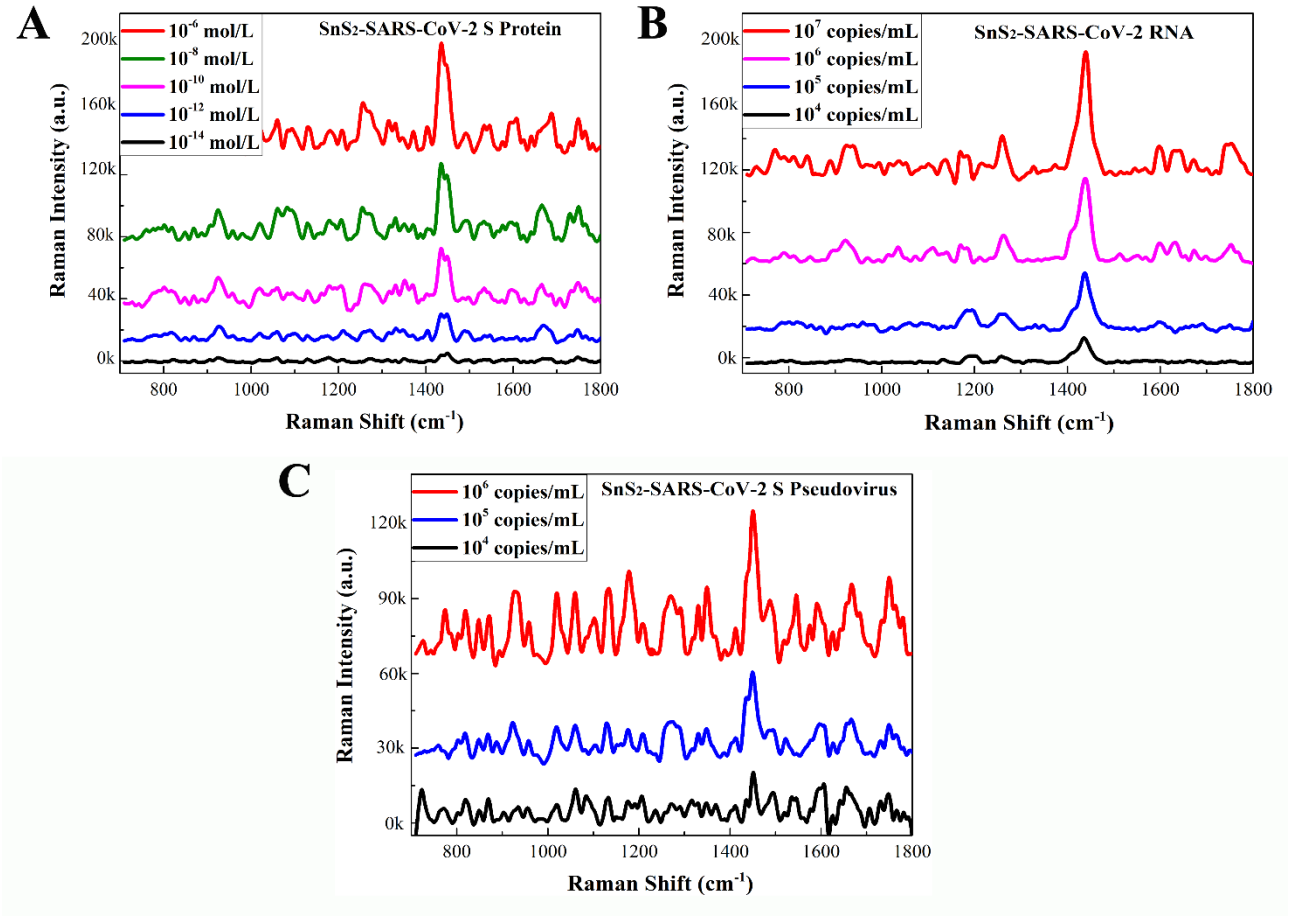

Figure S18. The limits of detection for three physical forms of SARS-CoV-2 virus.

(A) Raman spectra of 10^{-6}-10^{-14} mol/L SARS-CoV-2 S protein on SnS_2 microspheres.

(B) Raman spectra of 10^{4}-10^{7} copies/mL SARS-CoV-2 RNA on SnS_2 microspheres.

(C) Raman spectra of 10^{4}-10^{6} copies/mL SARS-CoV-2 S pseudovirus on SnS_2 microspheres.

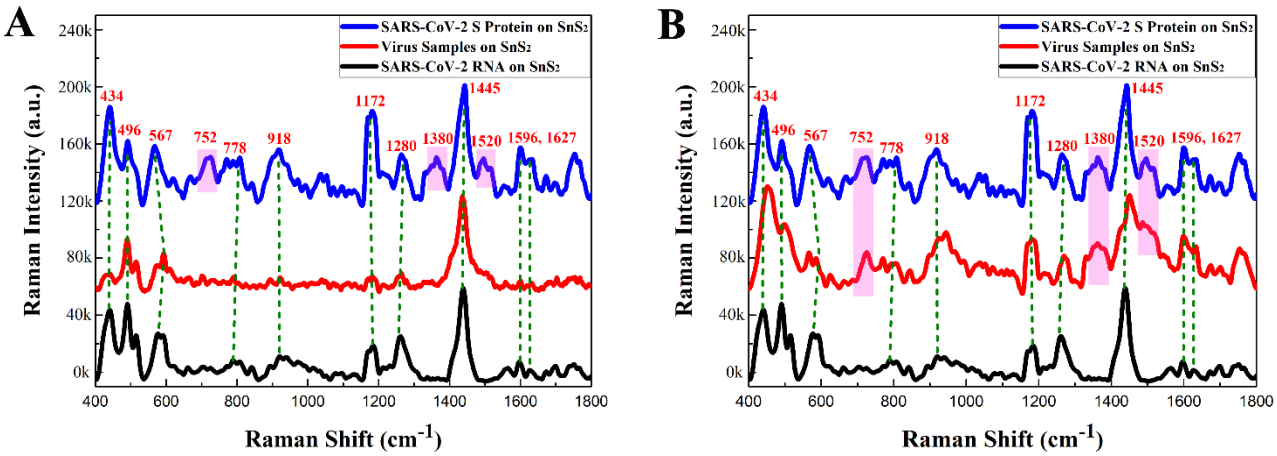

Figure S19. Comparison of Raman peaks for SARS-CoV-2 virus samples.

(A) Raman spectra of virus samples being identified to SARS-CoV-2 RNA.

(B) Raman spectra of virus samples SARS-CoV-2 being identified to SARS-CoV-2 S protein.

A

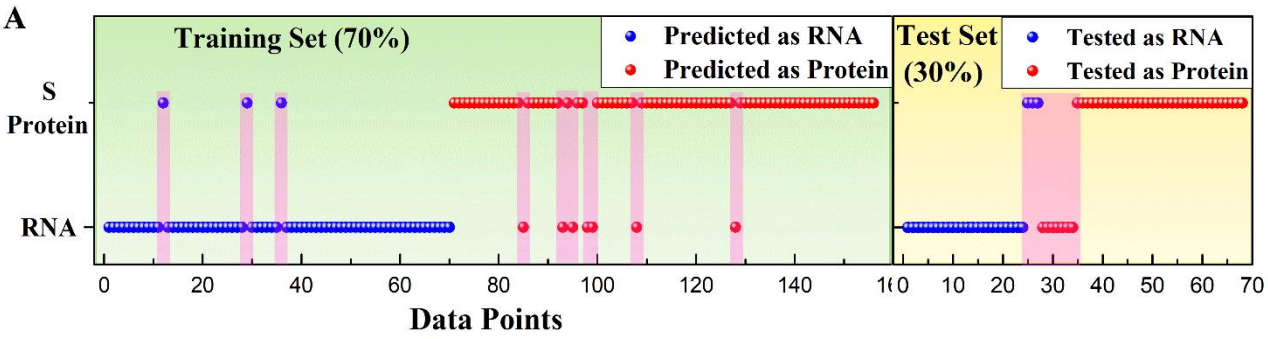

B

Classification		Training Set (70%)		Total	Test Set (30%)		Total
		Original Class			Original Class		
		RNA	S Protein		RNA	S Protein	
Predicted Class	RNA	67	7		24	7	
	S Protein	3	79		3	44	
	Accuracy	95.71%	91.86%	93.59%	88.89%	86.27%	85.29%

C

Classification Results			
Classification	Predicted Group		Total
	RNA	S Protein	
RNA	48	0	48
S Protein	0	31	31
Samples	57	98	156

Figure S20. The SVM analyzed results of virus sample with moderate infectious risk.

(A) Confusion matrix of SARS-CoV-2 S protein and RNA for the mixture of the complete-structure and the lysed SARS-CoV-2 after RNA elimination and re-lysis.

(B) Predicted labels of test set for SARS-CoV-2 S protein and RNA for the complete-structure and the lysed SARS-CoV-2 after RNA elimination and re-lysis.

(C) Classification results of viral samples for SARS-CoV-2 S protein and RNA based on Support Vector Machine (SVM) method.

A

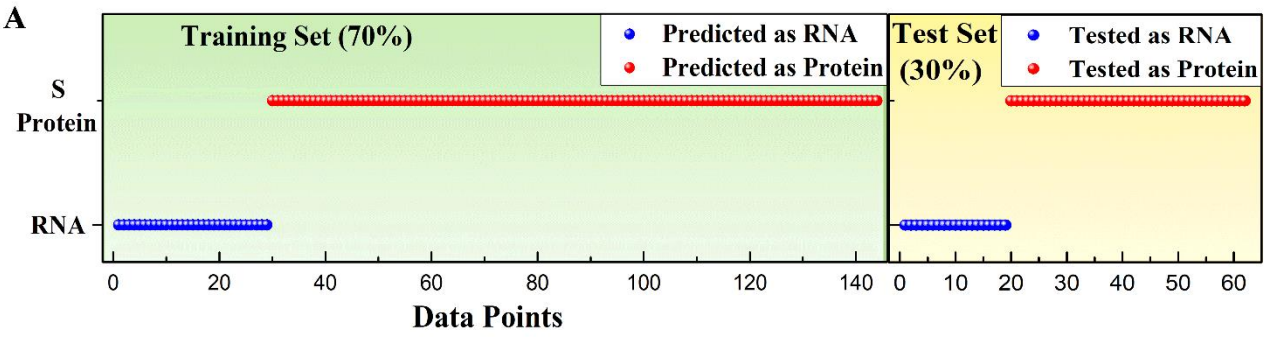

B

Classification		Training Set (70%)		Total	Test Set (30%)		Total
		Original Class			Original Class		
		RNA	S Protein		RNA	S Protein	
Predicted Class	RNA	29	0		19	0	
	S Protein	0	115		0	43	
	Accuracy	100.0%	100.0%	100.0%	100.0%	100.0%	100.0%

C

Classification Results			
Classification	Predicted Group		Total
	RNA	S Protein	
RNA	48	0	48
S Protein	0	31	31
Samples	0	127	127

Figure S21. The SVM analyzed results of virus sample with non-infectious risk.

(A) Confusion matrix of SARS-CoV-2 S protein and RNA for the lysed SARS-CoV-2 after RNA elimination and re-lysis.

(B) Predicted labels of test set for SARS-CoV-2 S protein and RNA for the lysed SARS-CoV-2 after RNA elimination and re-lysis.

(C) Classification results of viral samples for SARS-CoV-2 S protein and RNA based on Support Vector Machine (SVM) method.

SI-1. Raman vibration modes and SERS EFs of MeB

Table S1. Raman shifts of SERS characteristic peaks and corresponding assignments and EFs.

Raman shift (cm^{-1}) of MeB	**EF**	**Assignments**
1620	3.0×10^8	ν_{as} $(CCC)_{ring}$
1405	5.0×10^7	ν_s(C-N)
1182	6.0×10^7	ρ_τ(C-H)
1072	1.3×10^{10}	ρ_{ipb} $(CC_{center}C)$
772	5.5×10^7	$\nu_{as}(CN_{center}C)$

ν, stretching; ρ_τ, twisting vibrations; ρ_{ipb}, in-plane deformation; (s, symmetric; as, asymmetric)

SI-2. The calculation of enrichment multiples

In order to explore the physical enrichment of SnS_2 microspheres, we immersed SnS_2 powder in the MeB solution and dropped MeB solution on SnS_2 substrates for Raman detection. In detail, the 0.01 g of the synthesized SnS_2 microspheres was immersed in 30 mL of 10^{-7} M MeB aqueous solution and a dose of mixture solution with a volume of 5 μL after centrifugation was dropped on the surface of glass substrate, dried at room temperature for Raman detection. On another way, a volume of 5 μL for 10^{-7} M MeB solution was dropped on the synthesized SnS_2 microspheres substrates and dried at room temperature for Raman detection. Then, their Raman spectra were detected and the average number N_{SERS} of MeB molecules on SnS_2 microspheres in the Raman detection region was calculated to explore the physical enrichment of SnS_2 microspheres.

As for immersing SnS_2 powder in the 10^{-7} M MeB, $EF_1 = \frac{I_{SERS-1}}{I_{prob}} \times \frac{N_{prob}}{N_{SERS-1}}$;

As for dropping MeB on SnS_2 substrates, $EF_2 = \frac{I_{SERS-2}}{I_{prob}} \times \frac{N_{prob}}{N_{SERS-2}}$.

Theoretically, if we ignore the molecular enrichment effect, SnS_2 microspheres should show the same SERS enhancement factor for MeB molecule with the same concentration, that is $EF_1 = EF_2$.

$$\frac{I_{SERS-1}}{I_{prob}} \times \frac{N_{prob}}{N_{SERS-1}} = \frac{I_{SERS-2}}{I_{prob}} \times \frac{N_{prob}}{N_{SERS-2}}$$

$$\frac{N_{SERS-1}}{N_{SERS-2}} = \frac{I_{SERS-1}}{I_{SERS-2}} = \frac{4957650.07}{125098.17} \approx 40$$

Therefore, the physical enrichment of SnS_2 microspheres is $N_{SERS-1}/N_{SERS-2} = 40$.

SI-3. Enhancement factor (EF) calculations

SERS enhancement factors of SnS_2 microspheres substrates for MeB were calculated by the following general formula:

$$EF=\frac{I_{SERS}}{I_{prob}}\times\frac{N_{prob}}{N_{SERS}} \quad (1)$$

Based on formula (1), I_{SERS} and I_{prob} are the Raman intensity at a selected Raman peak of molecule-semiconductor complex and MeB probe molecules. N_{SERS} is the average number of MeB molecules on SnS_2 microspheres in the Raman detection region. N_{prob} is the average number of MeB powder in the Raman detection region. In the Raman scattering detection region.

As for the average number N_{SERS-1} of MeB molecules with SERS enhancement:

$$N_{SERS-1}=\frac{C_{sol}V_{sol}N_AA_{Raman}}{A_{substrate}} \quad (2)$$

As for the average number N_{SERS-2} of MeB molecules with SERS enhancement under the effect of molecular enrichment:

$$N_{SERS-2}=40\times N_{SERS-1}=\frac{40\times C_{sol}V_{sol}N_AA_{Raman}}{A_{substrate}} \quad (3)$$

As for the average number of MeB powder without SERS enhancemnt:

$$N_{prob}=C_{prob}hN_AA_{Raman} \quad (4)$$

Where C_{sol} (mol/L) is the concentration of the measured molecular solution, which is 10^{-13} M. And V_{sol} (L) is the volume of the solution that finally dropped on the glass slide after immersing MeB on SnS_2 microspheres powder, which is about 5 μL. A_{Raman} and $A_{substrate}$ (m^2) are the area of laser radiation and droplet diffusion of MeB and SnS_2 microspheres powder complex on the glass slide, respectively. And the circle diameter of droplet diffusion for MeB and SnS_2 microspheres powder complex is 0.8 cm. C_{prob} of MeB powder is 3.13 M. h is the laser radiation depth, which is 21 μm.[1]

$$\frac{N_{prob}}{N_{SERS-2}}=\frac{C_{prob}hN_AA_{Raman}A_{substrate}}{40\times C_{sol}V_{sol}N_AA_{Raman}}=\frac{C_{prob}hA_{substrate}}{C_{sol}V_{sol}}$$

$$=\frac{3.13\times 2.1\times 10^{-5}\times\pi\times 0.16\times 10^{-4}}{40\times 5\times 10^{-6}\times 10^{-13}}=1.66\times 10^{8}$$

Under the excitation of 785 nm laser, the Raman intensity I_{prob} of MeB powder at 1620 cm^{-1} is 201710.8, and I_{SERS} of MeB molecules with SERS enhancement at 1620 cm^{-1} is 363575.4. All Raman spectra complex were detected with the following test conditions: the irradiation power of excitation light is 300 mW×0.05% of 785 nm, and the light irradiation time of each point is 20 s, as well as the light transmission efficiency of the Raman spectrometer is about 20%. Therefore,

$$EF=\frac{I_{SERS}}{I_{prob}}\times\frac{N_{prob}}{N_{SERS}}=\frac{363575.4}{201710.8}\times 1.66\times 10^{8}=3.0\times 10^{8}$$

Based on above calculations of our works, SERS enhancement factors and the corresponding detection limits of all reported semiconductor-based SERS substrates were summarized in the following table.

Table S2. Reported enhancement factors on different semiconductor nanostructure substrates.

SERS substrates	**Probe molecules**	**Excitation wavelength (nm)**	**EF**	**Detection limits**
Multi-layer Nb_2C MXenes[2]	MeB	532	3.0×10^6	10^{-8} M
Multi-layer Ta_2C MXenes[2]	MV	532	1.4×10^6	10^{-7} M
Multi-layer Ti_3C_2 MXenes[3]	MeB	785	3.2×10^6	10^{-7} M
Monolayer of Ti_3C_2 MXene[4]	R6G	532	3.82×10^8	10^{-11} M
ZnSe nanoparticles[5]	4-Mpy	514.5	2×10^6	10^{-3} M
Amorphous TiO_2 nanosheets[6]	4-MBA	633	1.86×10^6	6×10^{-6} M
sea urchin-like $W_{18}O_{49}$[7]	R6G	532.8	3.4×10^5	10^{-7} M
Porous ZnO nanosheets[8]	4-MBA	514.5	10^3	10^{-6} M
Amorphous MoO_3[9]	R6G	532	1.8×10^7	10^{-8} M
Nanosphere Cu_2O[10]	R6G	514.5	8×10^5	6×10^{-9} M
Mo-doping Ta_2O_5 nanowires[1]	MV	532	2.2×10^7	9×10^{-9} M
Nb_2O_5 nanoflowers[11]	MV	532	7.1×10^7	10^{-8} M
Amorphous Rh_3S_6 microbowls[12]	R6G	647	10^5	10^{-7} M
Metal-Like $H_{1.68}MoO_3$[13]	R6G	633	1.1×10^7	10^{-9} M
Mo_2N flexible membrane[14]	2,4-DCP	532	5.2×10^7	10^{-11} M
MoN nanosheets[15]	R6G	633	8.2×10^6	10^{-10} M
$NbTe_2$ nanosheets[16]	MB	514	5.6×10^6	10^{-9} M
MoS_2@ZnO heterojunction[17]	MB	514	1.2×10^6	10^{-12} M
SnS_2 microspheres (in this work)	MeB	785	3.0×10^8	10^{-13} M

SI-4. Gene sequence of S protein for SARS-CoV-2 and SARS-CoV

The S protein of SARS-CoV-2 is similar to that of SARS-CoV, showing only 74.6% identity in their amino acid sequences. Their SERS spectra exhibit significant different characteristics peaks.

Gene sequence of SARS-CoV-2 S protein (Accession: YP_009724390.1)

MFVFLVLLPLVSSQCVNLTTRTQLPPAYTNSFTRGVYYPDKVFRSSVLHSTQDLFLPFFSNVTWFHAIHVSGTN
GTKRFDNPVLPFNDGVYFASTEKSNIIRGWIFGTTLDSKTQSLLIVNNATNVVIKVCEFQFCNDPFLGVYYHKN
NKSWMESEFRVYSSANNCTFEYVSQPFLMDLEGKQGNFKNLREFVFKNIDGYFKIYSKHTPINLVRDLPQGFS
ALEPLVDLPIGINITRFQTLLALHRSYLTPGDSSSGWTAGAAAYYVGVLQPRTFLLKYNENGTITDAVDCALDP
LSETKCTLKSFTVEKGIYQTSNFRVQPTESIVRFPNITNLCPFGEVFNATRFASVYAWNRKRISNCVADYSVLYN
SASFSTFKCYGVSPTKLNDLCFTNVYADSFVIRGDEVRQIAPGQTGKIADYNYKLPDDFTGCVIAWNSNNLDS
KVGGNYNYLYRLFRKSNLKPFERDISTEIYQAGSTPCNGVEGFNCYFPLQSYGFQPTNGVGYQPYRVVVLSFE
LLHAPATVCGPKKSTNLVKGCVIAWNSNNLDSKVGGNYNYLYRLFRKSNLKPFERDISTEIYQAGSTPCNGVE
GFNCYFPLQSYGFQPTNGVGYQPYRVVVLSFELLHAPATVCGPKKSTNLVKNKCVNFNFNGLTGTGVLTESN
KKFLPFQQFGRDIADTTDAVRDPQTLEILDITPCSFGGVSVITPGTNTSNQVAVLYQDVNCTEVPVAIHADQLTP
TWRVYSTGSNVFQTRAGCLIGAEHVNNSYECDIPIGAGICASYQTQTNSPRRARSVASQSIIAYTMSLGAENSV
AYSNNSIAIPTNFTISVTTEILPVSMTKTSVDCTMYICGDSTECSNLLLGYGSFCTQLNRALTGIAVEQDKNTQE
VFAQVKQIYKTPPIKDFGGFNFSQILPDPSKPSKRSFIEDLLFNKVTLADAGFIKQYGDCLGDIAARDLICAQKFN
GLTVLPPLLTDEMIAQYTSALLAGTITSGWTFGAGAALQIPFAMQMAYRFNGIGVTQNVLYENQKLIANQFNS
AIGKIQDSLSSTASALGKLQDVVNQNAQALNTLVKQLSSNFGAISSVLNDILSRLDKVEAEVQIDRLITGRLQSL
QTYVTQQLIRAAEIRASANLAATKMSECVLGQSKRVDFCGKGYHLMSFPQSAPHGVVFLHVTYVPAQEKNFT
TAPAICHDGKAHFPREGVFVSNGTHWFVTQRNFYEPQIITTDNTFVSGNCDVVIG
IVNNTVYDPLQPELDSFKEELDKYFKNHTSPDVDLGDISGINASVVNIQKEIDRLNEVAKNLNESLIDLQELGKY
EQYIKWPWYIWLGFIAGLIAIVMVTIMLCCMTSCCSCLKGCCSCGSCCKFDEDDSEPVLKGVKLHYT

Gene sequence of SARS-CoV S protein (Accession: YP_009825051.1)

MFIFLLFLTLTSGSDLDRCTTFDDVQBNVTQHTSSMRGVYYPDEIFRSDTLYLTQDLFLPFYSNVTGFHTINHTF
GNPVIPFKDGIYFAATEKSNVVRGWVFGSTMNNKSQSVIIINNSTNVVIRACNFELCDNPFFAVSKPMGTQTHT
MIFDNAFNCTFEYISDAFSLDVSEKSGNFKHLREFVFKNKDGFLVVVKGYQPIDVVRDLPSGFNTLKPIFKLPLG
INITNFRAILTAFSPAQDIWGTSAAAVFVGYLKPTTFMLKYDENGTITDAVDCSQNPLAELKCSVKSFEIDKGIY
QTSNFRVVPSGDVVRFPNITNLCPFGEVFNATKFPSVVAWERKKISNCVADYSVLYNSTFFSTFKCYGVSATKL
NDLCFSNVYADSFVVKGDDVRQIAPGQTGVIADYNYKLPDDFMGCVLAWNTRNIDATSTGNYNYKYRYLRH
GKLRPFERDISNVPFSPDGKPCTPALNCYWPLNDYGFYTTTGIGYQPYRVVVLSFELLNAPATVCGPKLSTDLI
KNQCVNFNFNGLTGTGVLTPSSKRFQPFQQFGRDVSDFTDSVRDPKTSEILDISPCAFGGVSVITPGTNASSEVA
VLYQDVNCTDVSTAIHADQLTPAWRIYSTGNNVFQTQAGCLIGAEHVDTSYECDIPIGAGICASYHTVSLLRST
SQKSIVAYTMSLGADSSIAYSNNTIAIPTNFSISITTEVMPVSMAKTSVDCNMYICGDSTECANLLLQYGSFCTQ
LNRALSGIAAEQDRNTREVFAQVKQMYKTPTLKYFGGFNFSQILPDPLKPTKRSFIEDLLFNKVTLADAGFMK
QVGECLGDINARDLICAQKFNGLTVLPPLLTDDMIAAYTAALVSGTATAGWTFGAGAALQIPFAMQMAYRFN
GIGVTQNVLYENQKQIANQFNKAISQIQESLTTTSTALGKLQDVVNQNAQALNTLVKQLSSNFGAISSVLNDIL
SRLDKVEAEVQIDRLITQRLQSLQTYVTQQLIRAAEIRASANLAATKMSECVLGQSKRVDFCGKGYHLMSFPQ
AAPHGVVFLHVTYVPSQERNFTTAPAICHEGKAYFPREGVFNGTSWFITQRNFFSPQIITTDNTFVSGNCDVVIG

IINNTVYDPLQPELDSFKEELDKYFKNHTSPDVDLGDISGINASVVNIQKEIDRLNEVAKNLNESLIDLQELGKY
EQVIKWPWYVWLGFIAGLIAIVMVTILLCCMTSCCSCLKGACSCGSCCKFDEDDSEPVLKGVKLHYT

Table S3. Raman peak assignments for proteins and virus on GNAs substrates

Assignments (Literature)	**Literature /(cm^{-1})**	**Reference Au /(cm^{-1})**	**Experiment SnS_2 /(cm^{-1})**
Protonated amine group, δ(-NH_3^+)	Ref[20]	454	434
δ(S-S)	518[20]	/	496
Amide V	567[19]	568	567
Trp, v(ϕ)	758[18]	752	752
Cys, v(C-C-N)	840[23]	/	778
Skeleton, v(C-C, α-Helix)	Ref[20]	950	918
Trp & Phe, v(C-C_6H_5)	1209[18]	1214	1172
Amide III, v (C-N), δ (N-H)	1300[21]	1296	1280
Trp, W7 [v(N_1–C_8)]	1365[19]	1380	1380
Nucleic Acids (DNA or RNA), proteins and lipids, v (C-H), b (N-H)	1450-1470[18,20]	1445	1445
Amide II, ρ_{ipb} (N-H, C-O)	1515[21] 1509-1552, 1529[22]	1521	1520
Tyr & Phe, v(ϕ)	1591[20]	1592	1596
v(C=C)	1617-1680[18]	1626	1627

Abbreviation: δ, deformation; v, stretching; ρ_{τ}, twisting vibrations; ϕ, aromatic ring; ρ_{ipb}, in-plane deformation; B bending vibration

SI-5. The definition of three existed forms for SARS-CoV-2 in this work

In this work, we defined three forms of SARS-CoV-2 virus and descripted their characteristics of viral structure.

(1) The active or un-lysed SARS-CoV-2 means that the virus has not been heated treatment, which exhibits a complete viral structure and high viral infectivity (as shown in the Schematic diagram A below). And its Raman spectra shows the characteristic Raman peaks of SARS-CoV-2 S protein.

(2) The SARS-CoV-2 with complete viral structure means that the virus has been heated at 45 ℃ for 10 min. Its spatial configuration and surface protein structure are still maintaining, only the viral activity and infectivity are reduced (as shown in the Schematic diagram B below). It is an incompletely inactivated virus, and its Raman spectra shows the characteristic Raman peaks of SARS-CoV-2 S protein.

(3) The lysed SARS-CoV-2 means that the virus was treated by the lysing process of ultrasound, whose virus structure and spatial configuration are destroyed, and the nucleic acids (RNA) and other proteins originally wrapped in the envelope are exposed or released outside the virus particle (as shown in the Schematic diagram C below). This lysed SARS-CoV-2 sample is non-infectious, and presents both the characteristic Raman peaks of SARS-CoV-2 S protein and RNA.

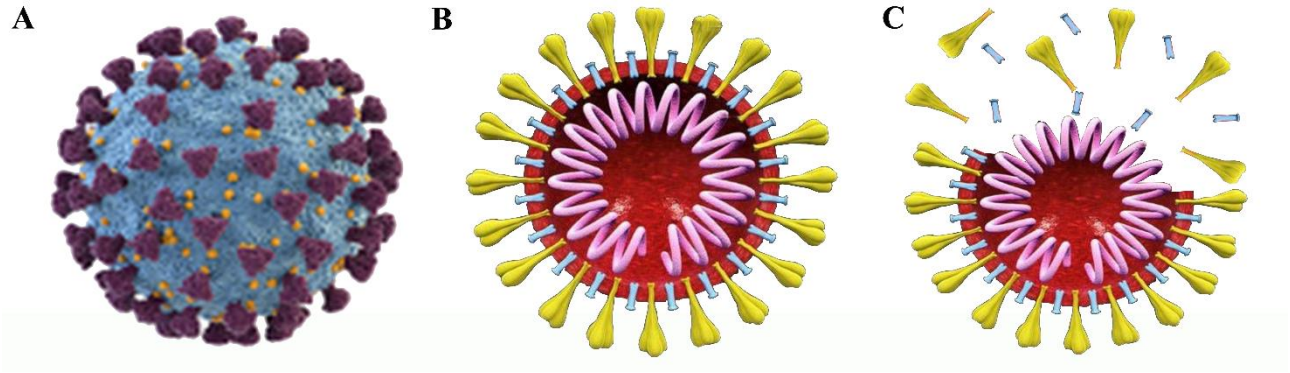

Schematic diagram of composition and structure for the active or un-lysed SARS-CoV-2 (A), the SARS-CoV-2 with complete viral structure (B), the lysed SARS-CoV-2 (C).

II-Supplemental Experimental Procedures

Preparation of SnS_2 microspheres

SnS_2 microspheres were synthesized through a simple one-step hydrothermal reaction with no surfactant or template agent adding. The microspheres morphology are directly formed by curling nanosheets through adjusting the concentration of reactants. Firstly, 1.6 g of thioacetamide (TTA) was dissolved in 55 mL of deionized water under electromagnetic stirring at 60 °C for about 10 minutes, and obtained a mixed transparent solution. The chemical reaction in this dissolution process is $CH_3CSNH_2 + H_2O = CH_3CONH_2 + H_2S$. Then, 0.8 g of $Na_2SnO_3{\cdot}3H_2O$ powder was dissolved in the above TTA solution, and mixed uniformly by electromagnetic stirring to obtain a precursor solution. Finally, above precursor solution was transferred into a 100 mL of PPL-lined stainless-steel autoclave to carry out the hydrothermal reaction at 180 ℃ for 24 hours, and obtain a brown precipitate. The brown precipitate was centrifuged, washed three times with deionized water, and freeze-dried to obtain the brown SnS_2 microspheres powder. The chemical reaction in the hydrothermal reaction is $Na_2SnO_3 + 2H_2S = SnS_2\downarrow + 2NaOH + H_2O$. In the entire hydrothermal reaction, $Na_2SnO_3{\cdot}3H_2O$ provides the Sn source, and thioacetamide provides the S source.

Characterizations

The powder X-ray diffraction (XRD) measurements of SnS_2 microspheres were carried out by using the Rigaku D/MAX-2200 PC XRD system (parameters: Cu Kα radiation, λ = 1.54 Å, 40 mA and 40 kV). The FEI Magellan 400 field emission scanning electron microscopy (FESEM) was used to provide the micro-morphology of SnS_2 microspheres. The transmission electron microscopy (TEM), high-resolution TEM (HRTEM), energy-dispersive X-ray spectroscopy (EDS) and selected area electron diffraction (SAED) images were performed on a JEM-2100F field emission source transmission electron microscope (200 kV). The Thermo Fisher Scientific ESCAlab250 provided the X-ray photoelectron spectroscopy (XPS).

Samples of the SARS-CoV-2 with complete viral structure and the lysed SARS-CoV-2 for TEM analysis were prepared by depositing 5 μl of diluted virions on the processed microvesicle copper net, and then negatively dyed with 1 wt% uranyl acetate solution for 90 sec and dried again. The stained samples were captured by 120 kV scanning transmission electron microscopes (FEI Titan S/TEM) at the Core Facility Center for Life Sciences, University of Science and Technology of China.

SERS measurements

The MeB aqueous solution with the different concentration of 10^{-6}-10^{-13} M were used to investigate the SERS performance of SnS_2 microspheres. For each Raman test, the 0.01 g of synthesized sample powder was immersed in 30 mL of molecule aqueous solution and treated with ultrasound for 2 h. A dose of mixture solution with a volume of 5 μL was dropped on the surface of glass substrate and dried at room temperature. All the Raman spectra of dye molecules were obtained by Renishaw inVia Reflex Raman spectrometer with the laser power of 0.15 mW at 785 nm and the accumulation time was 20 s, and the laser beam was focused to a spot about 1 μm in diameter with a 50× microscope objective. At least three different points on each substrate were tested, and selected the medium intensity of the Raman spectra at 1620 cm^{-1} peak to calculate the SERS EF value and analyze the relationship trend between the Raman intensity and the MeB concentration.

First-principles calculation

The first-principles calculations based on density functional theory (DFT)[24] with the CASTEP program are employed to investigate the electronic structure of SnS_2 hexagonal crystal with lattice strain and sulfur vacancies. Firstly, the supercell expansion of $3 \times 3 \times 1$ for SnS_2 hexagonal crystal structures with lattice strain from 0% to 20% and sulfur

vacancies were built. After geometry optimization, the band structure and density of states were calculated. During the calculation process, we adopted the PBE method in the generalized gradient approximation (GGA) to describe the periodic boundary conditions and the inter-electronic exchange-correlation energy[25]. The interaction potential between ion core and valence electrons was achieved by the ultra-soft potential (Ultrasoft). The cut-off energy of 600 eV in the wave vector K-space and the Brillouin zone of $4 \times 4 \times 5$ was chosen according to the special K-point of Monkhorst-Park[26]. The calculation accuracy of the crystal structure system reaching the convergence state is set as follows: the total energy change of the system stable within 10^{-6} eV, the force acting on each atom in the unit cell less than 0.005 eV/Å, the residual stress of the unit cell and the tolerance deviation within 0.02 GPa and 10^{-3} Å, respectively.

Machine-learning method based on PCA and Support Vector Machine (SVM)

The Python and Statistical Product & Service Solutions were used to perform Principal Component Analysis (PCA) between SARS-CoV-2 S protein and SARS-CoV S protein, SARS-CoV-2 RNA and SARS-CoV-2. According to PCA, we can get the main difference of Raman spectra for various physical forms of SARS-CoV-2 and constructed the identification standard between SARS-CoV-2 RNA and SARS-CoV-2 S protein. Then, Support Vector Machine (SVM) was used to classify the unknown-structure SARS-CoV-2 virus samples based on the above identification standard. Here we take 70% and 30% of the training set and test set, respectively. Polynomial kernel function, RBF kernel function and Linear kernel function are chosen to cross-validate the training data and select the linear kernel function with the highest accuracy.

SERS detection for five physical forms of SARS-CoV-2

With respect to the Raman detection for various physical forms of SARS-CoV-2, 5×10^{6} copies/mL of SARS-CoV-2 S pseudovirus, 1.33×10^{-6} mol/L of SARS-CoV-2 S protein, 7.47×10^{-7} mol/L of SARS-CoV S protein, about 10^{7} copies/mL of SARS-CoV-2 RNA and SARS-CoV-2 were detected by absorbing on SnS_2 microspheres substrates. Here, the 2.38 mg/mL of SARS-CoV-2 S protein, 3.73 mg/mL solution of SARS-CoV S protein were purchased from Sanyou Biopharmaceuticals (20 μg/Tube, Shanghai, China) and diluted to 1.5 mL by adding Phosphate-Buffered Saline (PBS) solution. Anhui Provincial Center for Disease Control and Prevention provided the 5×10^{6} copies/mL of SARS-CoV-2 S pseudovirus, 10^{9} copies/mL of SARS-CoV-2 RNA and SARS-CoV-2 and diluted to the concentration of 10^{7} copies/mL by adding non-nuclear water. Then, 0.01 g of SnS_2 powder was immersed in above 50 μL diluted biomolecular solutions of SARS-CoV-2 for 30 min and a dose of mixture solution with a volume of 5 μL after centrifugation process was dropped on the surface of glass substrate for Raman detection.

Preparation procedures of SARS-CoV-2 S pseudovirus and heating treatments of SARS-CoV-2

The production and purification of SARS-CoV-2 spike protein-based pseudovirions is shown below. As shown in the Schematic diagram below, Pseudovirions were produced by co-transfection of 293T cells with SARS-CoV-2 Spike protein expressing vector pcDNA3.1(+)-Opt-S and packaging vector pNL4-3-luc+R-E- through polyetherimide (PEI). The supernatants were harvested at 48 h post-transfection, passed through 0.45 μm filter and centrifuged at 800 × g for 5 min to remove cell debris. In order to get purer pseudovirions, 5×PEG8000 NaCl solution was added to the collected pseudovirions, left at 4℃ overnight, and centrifuged at 4000 g for 20 min next day. The supernatant was finally removed and collected by using 40 μl PBS solution.

According to the reported literature[27], the heating treatment at 45 ℃ for 10 min was adopted to reduce the viral activity and infectivity of SARS-CoV-2. The active SARS-CoV-2 samples came from COVID-19 patients were isolated and cultured in the BSL-3 laboratory and frozen at -80 ℃. It is worthwhile to note that all experiments on SARS-CoV-2 are required to be carried out in the P3 laboratory of Anhui Provincial Center for Disease Control and Prevention.

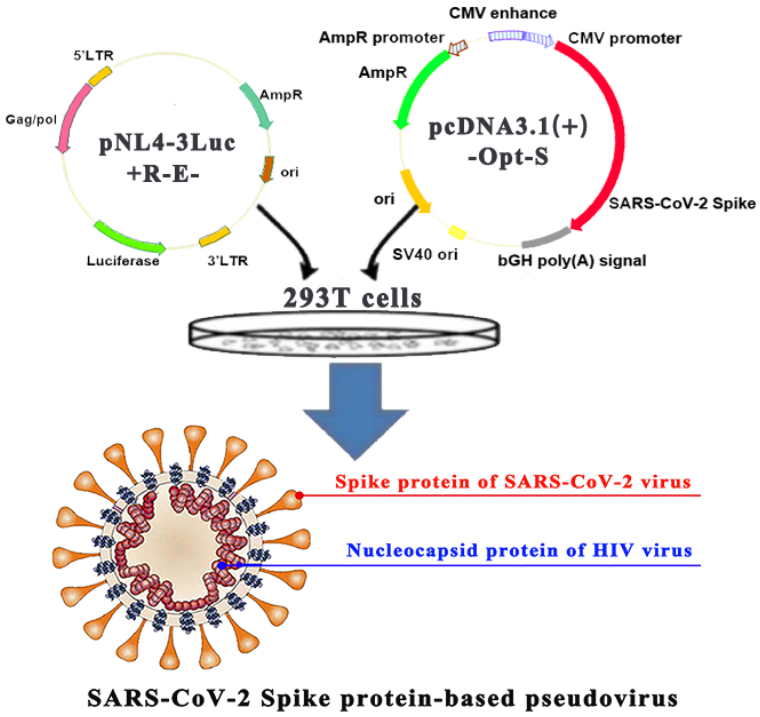

Schematic diagram of the spike protein-containing SARS-CoV-2 pseudovirus.

Exprimental procedures of indentifying the infectiousness of SARS-CoV-2 virus samples based on two-step SERS detections

Anhui Provincial Center for Disease Control and Prevention provided the 1 mL of SARS-CoV-2 with viral load of 10^7 copies/mL. This 1 mL of SARS-CoV-2 was divided into 200 μL, 600 μL, 200 μL, and transferred them to three centrifuge tubes named A, B, and C, respectively. The 600 μL of SARS-CoV-2 in B centrifuge tube was lysed by the lysing process of ultrasound to prepare the lysed SARS-CoV-2 sample. Then, 200 μL of the lysed SARS-CoV-2 was transferred to centrifuge tube C and shaken to mix evenly with the 200 μL of SARS-CoV-2 to prepare the mixture sample of the complete-structure virus and the lysed virus. After the first SERS detection, SARS-CoV-2 with complete viral structure in centrifuge tube A can be identified, and this virus sample exhibits a much severe risk of infectivity. And the infectiousness of the other two virus samples in centrifuge tubes A and B that existing the lysed SARS-CoV-2 cannot be diagnosed at this moment. Therefore, the second Raman detection after RNA elimination and re-lysis was necessary. The TIANSeq RNA Clean Beads was adopted to eliminate SARS-CoV-2 RNA from the lysed SARS-CoV-2 mixture. Firstly, the 200 μL of the lysed SARS-CoV-2 sample and the mixture sample of the complete-structure virus and the lysed virus were transferred into two clean 1.5 mL centrifuge tubes. Then, the magnetic beads binding buffer RM, which has been equilibrated to room temperature, was shaken to mix evenly. And the 440 μL of magnetic beads binding buffer RM was separately transferred to the above-prepared two virus samples and shaken to be mixed evenly. Next, the mixed virus solution was centrifuged to the bottom of the centrifuge tube by the instantaneous centrifugation, and was placed on a magnetic stand for 2-5 min. After the SARS-CoV-2 RNA were completely absorbed by magnetic beads, the upper liquid was carefully aspirated into two other clean 1.5 mL centrifuge tubes. At this moment, the SARS-CoV-2 RNA was eliminated from the upper liquid. Finally, the above-prepared upper liquid was re-lysed by the lysing process of ultrasound. It is worthwhile to note that all experiments on SARS-CoV-2 are required to be carried out in the P2/P3 laboratory.

Supplemental References

1. Yang, L.L., Peng, Y.S., Yang, Y., Liu, J.J., Huang, H.L., Yu, B.H., Zhao, J.M., Lu, Y.L., Huang, Z.R., Li, Z.Y., Lombardi, J.R. (2019). A Novel Ultra-Sensitive Semiconductor SERS Substrate Boosted by the Coupled Resonance Effect. Adv. Sci. *6*, 1900310.
2. Peng, Y.S., Lin, C.L., Long, L., Masaki, T., Tang, M., Yang, L.L., Liu, J.J., Huang, Z.R., Li, Z.Y., Yang, Y. et al. (2021). Charge-Transfer Resonance and Electromagnetic Enhancement Synergistically Enabling MXenes with Excellent SERS Sensitivity for SARS-CoV-2 S Protein Detection. Nano-Micro Lett. *13*, 52.
3. Peng, Y.S., Cai, P. Yang, L.L., Liu, Y.Y., Zhu, L.F., Zhang, Q.Q., Liu, J.J., Huang, Z.R., and Yang, Y. (2020). Theoretical and Experimental Studies of Ti_3C_2 MXene for Surface-Enhanced Raman Spectroscopy-Based Sensing. ACS Omega *5*, 26486−26496.
4. Ye, Y.T., Yi, W.C., Liu, W., Zhou, Y., Bai, H., Li, J.F., Xi, G.C. (2020). Remarkable surface-enhanced Raman scattering of highly crystalline monolayer Ti_3C_2 nanosheets. Sci. China Mater. *63(5)*, 794–805.
5. Islam, S.K., Tamargo, M., Moug, R., and Lombardi, J. R. (2013). Surface-Enhanced Raman Scattering on a Chemically Etched ZnSe Surface. J. Phys. Chem. C *117*, 23372-23377.
6. Wang, X.T., Shi, W.X., Wang, S.X., Zhao, H.W., Lin, J., Yang, Z., Chen, M., Guo, L. (2019). Two-Dimensional Amorphous TiO_2 Nanosheets Enabling High-Efficiency Photoinduced Charge Transfer for Excellent SERS Activity. J. Am. Chem. Soc. *141*, 5856-5862.
7. Cong, S., Yuan, Y.Y., Chen, Z.G., Hou, J.Y., Yang, M., Su, Y.L., Zhang, Y.Y., Li, L., Li, Q.W., Geng, F.X., Zhao, Z.G. (2015). Noble metal-comparable SERS enhancement from semiconducting metal oxides by making oxygen vacancies. Nat. Commun. *6*, 7800.
8. Liu, Q., Jiang, L., and Guo, L. (2014). Precursor-directed self-assembly of porous ZnO nanosheets as high-performance surface-enhanced Raman scattering substrate. Small *10*, 48-51.
9. Wu, H., Wang, H., and Li, G. (2017). Metal oxide semiconductor SERS-active substrates by defect engineering. Analyst *142*, 326-335.
10. Lin, J., Shang, Y., Li, X.X., Yu, J., Wang, X.T., Guo, L. (2017). Ultra-sensitive SERS Detection by Defect Engineering on Single Cu_2O Superstructure Particle. Adv. Mater. *29*, 1604797.
11. Peng, Y.S., Lin, C.L., Tang, M., Yang, L.L., Yang, Y., Liu, J.J., Huang, Z.R., and Li, Z.Y. (2020). Niobium pentoxide ultra-thin nanosheets: A photocatalytic degradation and recyclable surface-enhanced Raman scattering substrate. Appl. Surf. Sci. *509*, 145376.
12. Li, A.R., Lin, J., Huang, Z., Wang, X.T., and Guo, L. (2018). Surface-Enhanced Raman Spectroscopy on Amorphous Semiconducting Rhodium Sulfide Microbowl Substrates. iScience *10*, 1-10.
13. Zhu, Q., Jiang, S.L., Ye, K., Hu, W., Zhang, J.C., Niu, X.Y., Lin, Y.X., Chen, S.M., Song, L., and Luo, Y. (2020). Hydrogen-Doping-Induced Metal-Like Ultra-high Free-Carrier Concentration in Metal-Oxide Material for Giant and Tunable Plasmon Resonance. Adv. Mater. *32*, 2004059.
14. Song, X.Y., Yi, W.C., Li, J.F., Kong, Q.H., Bai, H., and Xi, G.C. (2021). Selective Preparation of Mo_2N and MoN with High Surface Area for Flexible SERS Sensing. Nano Lett. *21*, 4410-4414.
15. Guan, H.M., Yi, W.C., Li, T., Li, Y.H., Li, J.F., Bai, H., and Xi, G.C. (2020). Low temperature synthesis of plasmonic molybdenum nitride nanosheets for surface enhanced Raman scattering. Nat. Commun. *11*, 3889.
16. Wang, K.K., Guo, Z.Y., Li, Y., Guo, Y.X., Liu, H., Zhang, W., Zou, Z.Z., Zhang, Y.L., and Liu, Z.M. (2020). Few-Layer $NbTe_2$ Nanosheets as Substrates for Surface-Enhanced Raman Scattering Analysis. ACS Appl. Nano Mater. *3(11)*, 11363–11371.

17. Quan,Y.N., Yao, J.C., Sun, Y.S., Qu, X., Su, R., Hu, M.Y., Chen, L., Liu, Y., Gao, M., and Yang, J.H. (2021). Enhanced semiconductor charge-transfer resonance: Unprecedented oxygen bidirectional strategy. Sens. Actuators, B *327,* 128903.
18. Aubrey, K.L. and Thomas, G.J. (1992). man spectroscopy of filamentous bacteriophage Ff (fd, M13, f1) incorporating specifically-deuterated alanine and tryptophan side chains. Assignments and structural interpretation. Biophys. J. *60(6),* 1337-1349.
19. Krimm, S. and Bandekar, J. (1986). Vibrational Spectroscopy and Conformation of Peptides, Polypeptides, and Proteins. Adv. Protein Chem. *38,* 181-364.
20. Miura, T. and Thomas, G.J. (1995). Raman Spectroscopy of Proteins and Their Assemblies. Subcell. Biochem. *24,* 55-99.
21. Bandekar, J. (1992). Amide Modes and Protein Conformation. Biochim. Biophys. Acta *1120(2),* 123-143.
22. Cardona, M. (1982). Light Scattering in Solids II, Chapter 2 Resonance Phenomena. (Springer Berlin Heidelberg).
23. Proniewicza, E., Tata, A., Starowicz, M., Wojcik, A., Pacek, J., and Molenda, M. (2021). Is the electrochemical or the "green chemistry" method the optimal method for the synthesis of ZnO nanoparticles for applications to biological material? Characterization and SERS on ZnO. Colloid Surf. A-Physicochem. Eng. Asp. *609,* 125771.
24. Hohenberg, P. and Kohn, W. (1964). Inhomogeneous Electron Gas. Phys. Rev. *136,* B864-B871.
25. Perdew, J.P., Burke, K., and Ernzerhof, M. (1996). Generalized Gradient Approximation Made Simple. Phys. Rev. Lett. *77,* 3865-3868.
26. Monkhorst, H.J. and Pack, J.D. (1976). Special points for Brillouin-zone integrations. Phys. Rev. B *13,* 5188-5192.
27. Ulloa, S., Bravo, C., Ramirez, E., Fasce, R., and Fernandez, J. (2021). Inactivation of SARS-CoV-2 isolates from lineages B.1.1.7 (Alpha), P.1 (Gamma) and B.1.110 by heating and UV irradiation. J. Virol. Methods *295,* 114216.